Metamorphic rocks with different pressure–temperature–time paths bounded by a ductile shear zone at Oyayubi ridge, Brattnipene, Sør Rondane Mountains, East Antarctica

Tatsuro ADACHI[*], Tetsuo KAWAKAMI[**], Fumiko HIGASHINO[**] and Masaoki UNO[***]

[*]*Division of Earth Sciences, Faculty of Social and Cultural Studies, Kyushu University, Fukuoka 819–0395, Japan*
[**]*Department of Geology and Mineralogy, Graduate School of Science, Kyoto University, Kyoto 606–8502, Japan*
[***]*Department of Geoscience and Technology, Graduate School of Engineering, Tohoku University, Sendai 980–9570, Japan*

The Sør Rondane Mountains, East Antarctica have been thought to be situated in the collision zone between East and West Gondwana during the final stage of amalgamation of the Gondwana supercontinent. They are, therefore, recognized as a key region for understanding the geological phenomena during the collisions and for testing the proposed tectonic models. We identified metamorphic rocks with different pressure–temperature–time paths that are bounded by a ductile shear zone at Oyayubi ridge, Brattnipene, Sør Rondane Mountains. Based on field and microscopic observations, chemical analyses of minerals, and zircon U–Pb dating, the sillimanite–garnet–biotite gneisses (i.e., pelitic gneisses) from higher structural level show a peak metamorphism at ~ 590 Ma that took place under conditions of ~ 830–840 °C and 0.8–0.9 GPa, and these high–temperature conditions lasted until ~ 550 Ma. These rocks underwent isothermal decompression and then retrograde hydration under lower pressure–temperature conditions than 530 °C and 0.4 GPa at ~ 530 Ma. In contrast, the orthogneisses that consist of hornblende–biotite gneiss and garnet–clinopyroxene gneiss from lower structural levels did not undergo metamorphism at ~ 600 Ma but underwent metamorphism at ~ 570 Ma and reached peak conditions of 700–760 °C and 0.6–0.9 GPa at ~ 560–550 Ma. These observations suggest thrusting of the pelitic gneiss over the orthogneiss at ~ 570–550 Ma, causing a prograde metamorphism of the orthogneisses and a decompression of the pelitic gneisses as well as uplift and subsequent rapid denudation. The results indicate two stages of collision in the Sør Rondane Mountains and that the ductile shear zone bounding the pelitic gneiss and orthogneiss units may have been part of the continental plate collision boundary at ~ 570–550 Ma.

Keywords: *P–T–t* path, Unit boundary, Sør Rondane Mountains, East Antarctica

INTRODUCTION

The Sør Rondane Mountains (SRM; 22°–28°E and 71.5°–72.5°S) in eastern Dronning Maud Land (DML), East Antarctica have been thought to be situated in the collision zone between East and West Gondwana during the final stage of amalgamation of the Gondwana supercontinent (e.g., Stern, 1994). Several orogenies have been proposed to explain the amalgamation of Gondwana (Figs. 1a and 1b). For example, Jacobs and Thomas (2004) proposed an East African–Antarctic Orogen (EAAO; Fig. 1a), which was an extension in Antarctica of the East African Orogen (EAO) of Stern (1994), and which constituted one huge orogenic belt that was active from ~ 650 to 500 Ma. On the other hand, Meert (2003) proposed two crossing orogens, with the East African Orogen active during 750–620 Ma and the Kuunga Orogen during 580–500 Ma (Fig. 1b). Since the SRM lie within an orogen in any model, they are recognized as a key region for understanding the geological phenomena during the collisions and for testing the proposed tectonic models. The tectonic models of the SRM are still under debate, with some interpretations close to those of Jacobs and Thomas (2004) (e.g., Osanai et al., 2013), others similar to those of Meert (2003) (e.g., Grantham et al., 2013; Tsukada et al., 2017), and with no consensus so far.

The SRM consist of high–grade metamorphic rocks, from which *P–T* paths and age data can be obtained from a single rock sample. These data allow us to trace the

doi:10.2465/jmps.230220
T. Adachi, t-adachi@scs.kyushu-u.ac.jp Corresponding author

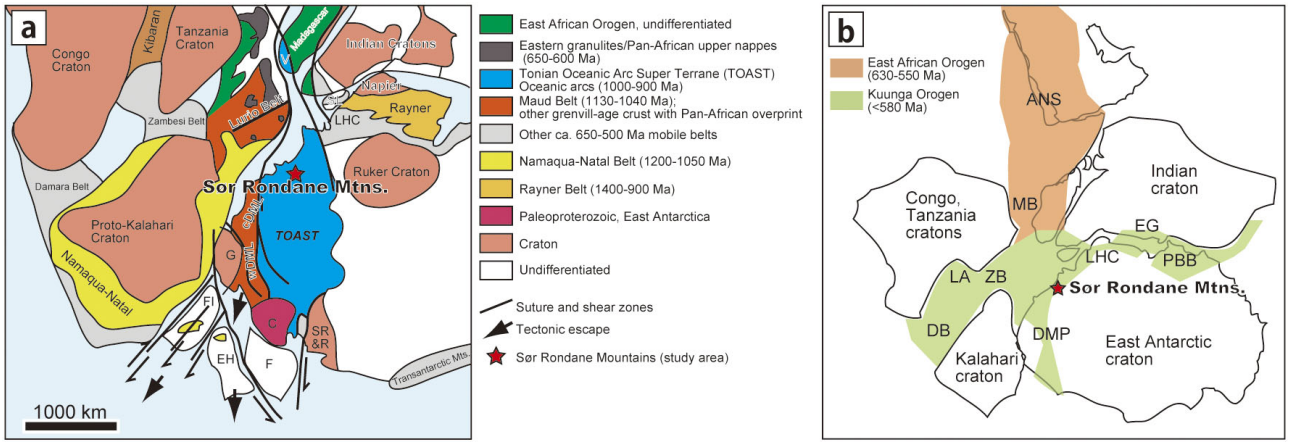

Figure 1. Geological context of the Sør Rondane Mountains (SRM). (a) Location of SRM in the East African–Antarctic Orogen (EAAO) (after Jacobs and Thomas, 2004; Jacobs et al., 2015). C, Coats Land; cDML, central Dronning Maud Land; EH, Ellsworth–Haag; F, Filchner block; FI, Falkland Islands; G, Grunehogna; LHC, Lützow–Holm Complex; M, Madagascar; R, Read Block; SL, Sri Lanka; SR, Shackleton Range; V, Vohibori; wDML, western Dronning Maud Land. (b) Location of SRM in the crossing orogenic belts (East Africa Orogen and Kuunga orogen) proposed by Meert (2003) (modified after Engvik et al., 2019). ANS, Arabian–Nubian Shield; DB, Damara Belt; DMP, Dronning Maud Province; EG, Eastern Ghats; LA, Lufilian Arc; LHC, Lützow–Holm Complex; MB, Mozambique Belt; PBB, Prydz Bay Belt; ZB, Zambezi Belt.

changing location of each sample in the crust over time, thus enabling us to understand the history of crustal movements during orogenies. *P–T–t* paths can also be used to recognize the extent of a single geological unit, because rocks in a single geological unit should share a common *P–T–t* path, while units with different *P–T–t* histories can be considered to have moved independently of each other. Thus, based on an analysis of *P–T–t* paths, it is possible to identify the extent of each geologic unit and to analyze the behavior of these units within the collisional zone, leading to the development of a precise tectonic model.

In this paper, based on field and microscopic observations, chemical analyses of minerals, and zircon U–Pb dating, we describe the *P–T–t* paths of pelitic gneisses and orthogneisses at Oyayubi ridge, Brattnipene, in the central SRM. We also discuss tectonic models of the formation of the SRM.

GEOLOGICAL OUTLINE

The SRM are composed mainly of late Proterozoic greenschist– to granulite–facies metamorphic rocks and later intrusions of granitoids and syenites (Fig. 2; e.g., Shiraishi et al., 1991, 1997). Mineral assemblages typical of ultrahigh–temperature metamorphism have been described recently from Balchenfjella by Higashino and Kawakami (2022). Pervasive Cl–rich fluid in the SRM has attracted attention because of the record of intense water–rock interaction (e.g., Higashino et al., 2013; Kawakami et al., 2017; Uno et al., 2017; Higashino et al., 2019; Mindaleva et al., 2020; Higashino et al., 2023). Based on the chemical composition of metamorphic rocks of igneous origin, the central part of the mountains has geochemical affinities with the oceanic, island arc, accretionary complex, and continental margin settings of modern plate tectonics (Osanai et al., 1992; Ishizuka et al., 1996). Detrital zircons from metamorphic rocks of sedimentary origin have dates that cluster around 3000, 2300–1900, and 1300–750 Ma (Kitano et al., 2016 and references therein). The apparent depositional ages of metacarbonates from Balchenfjella, Brattnipene, Menipa, and Tanngarden are estimated to be 880–850 Ma and 820–790 Ma, based on Sr isotope data (Otsuji et al., 2013). The dates of inherited zircons in metamorphosed igneous rocks cluster mainly around 1200–900 Ma, but with small clusters around 780 and 650 Ma (Kitano et al., 2016 and references therein). The igneous rocks in the SRM were formed in multiple stages. The metatonalites that dominate in the southwestern part of the mountains are categorized as low–K tholeiitic granitoids that formed at ~ 1000 Ma and low–K calc–alkaline adakites that formed at 950–920 and 770 Ma (Kamei et al., 2013; Elburg et al., 2015). Their chemical and isotopic compositions suggest a juvenile oceanic arc setting (Kamei et al., 2013; Elburg et al., 2015). High–Ti back–arc basin mafic magmatism occurred simultaneously with the early stage of calc–alkaline magmatism (Owada et al., 2013; Elburg et al., 2015). Jacobs et al. (2015) showed that the juvenile crust that formed at ~ 1000–900 Ma in the SRM extends to the eastern part of central DML, and they defined the entire distribution of this juvenile crust as the Tonian Oceanic Arc Super Terrane (TOAST).

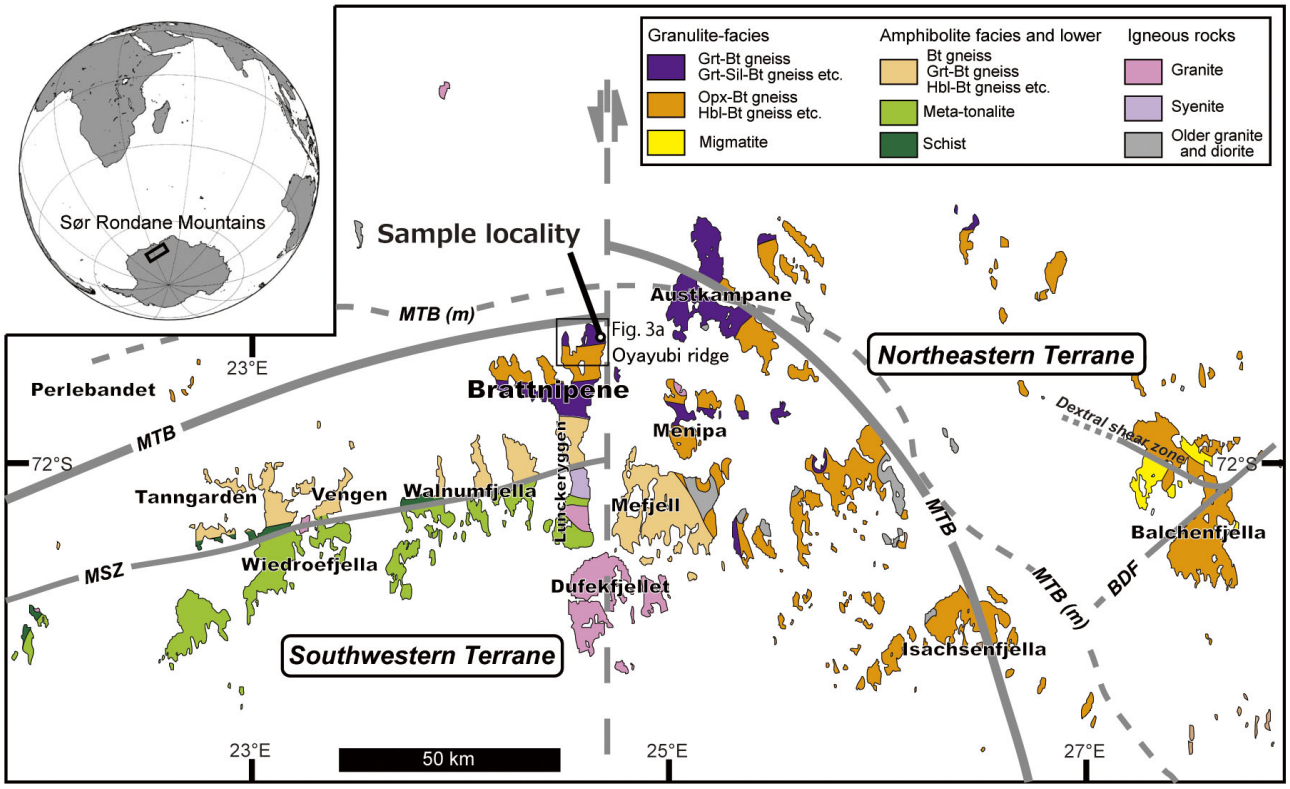

Figure 2. Geological outline map of the Sør Rondane Mountains, East Antarctica (modified after Osanai et al., 1992; Shiraishi et al., 1997; Osanai et al., 2013). The Main Tectonic Boundary (MTB) is after Osanai et al. (2013) and the MTB (m) is after Mieth et al. (2014). The Balchen Detachment Fault (BDF) is after Ishikawa et al. (2013). Sample locality and position of Oyayubi ridge are also shown.

The SRM have been divided into NE and SW Terranes separated by the Sør Rondane Suture, based on the areal distributions of rocks with different metamorphic grades (Osanai et al., 1992). This division has now been redefined, and the boundary between the two terranes is referred to as the Main Tectonic Boundary (MTB, Fig. 2; Osanai et al., 2013). According to this new terrane definition, each terrane has the following characteristics: the NE Terrane records a clockwise *P*–*T* path and reached peak conditions at 650–600 Ma (Shiraishi et al., 2008; Adachi et al., 2013a, 2013b; Hokada et al., 2022) and contains detrital zircons older than 1200 Ma (Kitano et al., 2016) while the SW Terrane records a counterclockwise *P*–*T* path with the timing of the peak conditions the same as for the NE Terrane (Shiraishi et al., 2008; Adachi et al., 2013a, 2013b; Baba et al., 2013; Nakano et al., 2013; Kawakami et al., 2017). Detrital zircons older than 1200 Ma have not been found in the SW Terrane (Kitano et al., 2016). Metatonalites are distributed in the southern part of the SW Terrane, and their northern limit is referred to as the Main Shear Zone (MSZ; Kojima and Shiraishi, 1986).

These metamorphic rocks are intruded by the following late- to post-tectonic granitoids: the ~ 640–600 Ma Dufek Granite; ~ 580–540 Ma leucogranites, pegmatites and minette; and ~ 530–500 Ma granites (Wang et al., 2020 and references therein). Post-kinematic mafic dikes represent the youngest intrusions in the area (Owada et al., 2008).

Toyoshima et al. (2013) investigated megascopic geological structures in the SRM. The predominant structural trends, based on a form-line contour map, are a compressional event between 600 and 560 Ma and subsequent horizontal extension. Ishikawa et al. (2013) described a dextral shear zone and the Balchen Detachment Fault (BDF) in Balchenfjella, in the eastern part of the SRM (Fig. 2). Extensional deformation related to the BDF took place between 600 and 550 Ma, and was interpreted to be the result of extensional collapse after crustal overthickening.

Based on these observations, Osanai et al. (2013) proposed a tectonic model in which the collision of the two terranes resulted in thrusting of the NE Terrane over the SW Terrane at 650–600 Ma, followed by retrograde metamorphism at 590–530 Ma. In this model, greenschist- to amphibolite-facies metamorphic rocks at Lunckeryggen, Vengen, and Wiedrøefjella have been interpreted as a shallow part of the SW Terrane that underwent peak amphibolite-facies metamorphism at 650–600 Ma and subsequent hydration and mylonitization (Osanai

et al., 2013). However, Adachi et al. (2013a) reported metamorphic ages of ~ 550 Ma for zircons from Lunckeryggen, and Adachi et al. (2013b) demonstrated a lack of metamorphic zircons with ages of ~ 650–600 Ma. Rocks without the latter ages occur sporadically in the SW Terrane (Asami et al., 2005; Shiraishi et al., 2008; Adachi et al., 2013b).

Grantham et al. (2008, 2013, 2019) proposed a different model involving the formation of a mega-nappe complex through northern and southern Gondwana as a result of collision during the 580–540 Ma Kuunga Orogeny. They considered that the hanging-wall of the mega-nappe comprises an accretionary thrust-fault stacked complex that was formed at ~ 640–600 Ma and which can be observed in the eastern part of the SRM. Tsukada et al. (2017) reported a low-angle brittle shear zone (Kanino-tsume Shear Zone, KSZ) in the western part of the SRM and proposed a similar tectonic model to that of Grantham et al. (2013). Based on the examination mainly of igneous rocks, Jacobs et al. (2020) and Wang et al. (2020) proposed a tectonic model in which the western and eastern DML were situated in two independent subduction zone systems until ~ 600 Ma. They proposed that the western DML formed the margin of the Kalahari Craton and that the eastern DML formed part of TOAST, with the two parts of the DML colliding after ~ 590–550 Ma.

Brattnipene is situated in the central part of the SRM, within the SW Terrane. This area is composed mainly of hornblende-biotite gneiss, garnet-biotite gneiss, biotite gneiss, and intercalated garnet-sillimanite-biotite gneiss, amphibolite, charnockitic gneiss, marble, and calcsilicate rock (Osanai et al., 1996). The gneisses in this area preserve textures indicating compression before peak metamorphic conditions that are estimated to have been ~ 800–900 °C and 0.8–0.9 GPa (Adachi et al., 2013a; Baba et al., 2013) at ~ 640–600 Ma (Shiraishi et al., 2008; Adachi et al., 2013b). Textures indicating retrograde hydration are common (Adachi et al., 2010, 2013a). Especially retrograde kyanite, which replaces garnet with biotite and sillimanite are characteristics of the pelitic gneisses in this area (Asami and Shiraishi, 1987; Asami et al., 1992; Adachi et al., 2013a). This hydration is considered to be related to magmatic activity at ~ 550 Ma (Shiraishi et al., 2008; Adachi et al., 2013b). Foliation and lithological boundaries have a monotonous E-W strike and dip to the S, except in the southern part of the area, where a large-scale fold zone is developed (Toyoshima et al., 2013).

ANALYTICAL METHODS

Quantitative analyses of minerals and X-ray elemental mapping were performed using an electron probe micro-analyzer (EPMA, JEOL JXA-8530F). The analytical conditions for the analyses, except for rutile, were an acceleration voltage of 15 kV, a 12 nA beam current, and a beam diameter of 2 μm. The measurement times for the peak and backgrounds were respectively 60 and 30 s for Cl, 90 and 45 s for F, and 10 and 5 s for other elements. Quantitative analyses of rutile followed the method of Zack et al. (2004), with an acceleration voltage of 15 kV and a beam diameter of 2 μm. Interferences from Ti $K\beta$ on V$K\alpha$ and V$K\beta$ on Cr$K\alpha$ were corrected additionally. Natural and synthetic minerals and metals were used as calibration standards, and ZAF corrections were applied. The analytical conditions for X-ray elemental mapping were an acceleration voltage of 15 kV, a probe current of 50–500 nA, a beam diameter of 3–10 μm, and a dwell time of 40 ms.

Analyses using laser Raman spectroscopy (JASCO NRS-3100) were performed with a 532 nm YAG laser at 30 mW to identify the Al_2SiO_5 minerals.

U-Pb dating of zircons that had been separated and placed in grain mounts was performed using an ArF excimer laser ablation system (LA, Photon Machines AnalyteG2) combined with a quadrupole inductively coupled plasma-mass spectrometer (ICP-MS, Agilent 7500cx), using a method based on Nakano et al. (2021). For in situ zircon U-Pb dating, we added ^{29}Si, ^{157}Gd, and ^{172}Yb to monitored isotopes to calculate the concentrations of ^{157}Gd, ^{172}Yb, ^{232}Th, and ^{238}U using ^{29}Si as an internal standard. The 91500 zircon (Wiedenbeck et al., 1995) was used as the calibration standard for the U-Pb dating. The FC-1 (Paces and Miller, 1993) and Temora2 (Black et al., 2003) standard zircons were analyzed for quality control. Time-dependent drifts of U-Th-Pb isotope ratios were corrected using a linear interpolation for every five analyses. A NIST SRM-611 glass was used to determine the ratios and concentrations of the trace elements. The data for the isotopic ratios and concentrations were processed using GLITTER software (Griffin et al., 2008) and plotted using Isoplot/Ex 4.15 software (Ludwig, 2012). All data uncertainties are reported at the 2σ confidence level. For separated grain mount analyses, the weighted mean ^{206}Pb–^{238}U ages for the FC-1 and Temora2 zircons were respectively 1102 ± 7 Ma (MSWD = 0.53, n = 24) and 420 ± 7 Ma (MSWD = 0.53, n = 24), and for in situ analyses they were 1100 ± 7 Ma (MSWD = 0.35, n = 18) and 418 ± 4 Ma (MSWD = 0.05, n = 17). The internal textures of the zircon grains were observed using a scanning electron microscope (SEM, JEOL JSM-5301S) with a cathodoluminescence (CL) detector (Gatan MiniCL).

All the analyses described above were undertaken at Kyushu University, Japan.

SAMPLE LOCATIONS AND DESCRIPTIONS, AND MINERAL CHEMISTRY

The samples analyzed in this study were collected on the eastern slope of Oyayubi ridge, Brattnipene (Figs. 2 and 3a), during the summer season of the 61st Japanese Antarctic Research Expedition (JARE61; Kawakami et al., 2020). At this locality, pelitic gneisses (sillimanite–garnet–biotite gneisses) overlie orthogneisses (hornblende–biotite gneiss and garnet–clinopyroxene gneiss) along a low-angle ductile shear zone (Figs. 3b and 3c). The foliation in the gneisses strikes E–W and dips gently (~ 20°) north. The lineation plunges gently (~ 20°) to the WNW. The orthogneisses are truncated by deformed pegmatites and undeformed leucocratic veins (Fig. 3d). Detailed descriptions of the studied samples are given below and in Figures 4–6. The chemical compositions of the minerals are shown in Figure 7. Representative mineral compositions are provided in Supplementary Tables S1 and S2 (Tables S1–S4 are available online from https://doi.org/10.2465/jmps.230220). The calculations of hornblende and biotite chemical formulae, including estimations of Fe^{3+}, are based on the methods of Leake et al. (1997) and Guidotti and Dyar (1991), respectively. The abbreviations used in this study follow Whitney and Evans (2010) and those related to chemical compositions are defined as follows: $X_{Mg} = Mg/(Mg + Fe^{2+})$, An = Ca/(Ca + Na + K) × 100, Ab = Na/(Ca + Na + K) × 100, Or = K/(Ca + Na + K) × 100, Alm = Fe^{2+}/(Fe^{2+} + Mg + Mn + Ca) × 100, Prp = Mg/(Fe^{2+} + Mg + Mn + Ca) × 100, Sps = Mn/(Fe^{2+} + Mg + Mn + Ca) × 100, and Grs = Ca/(Fe^{2+} + Mg + Mn + Ca) × 100.

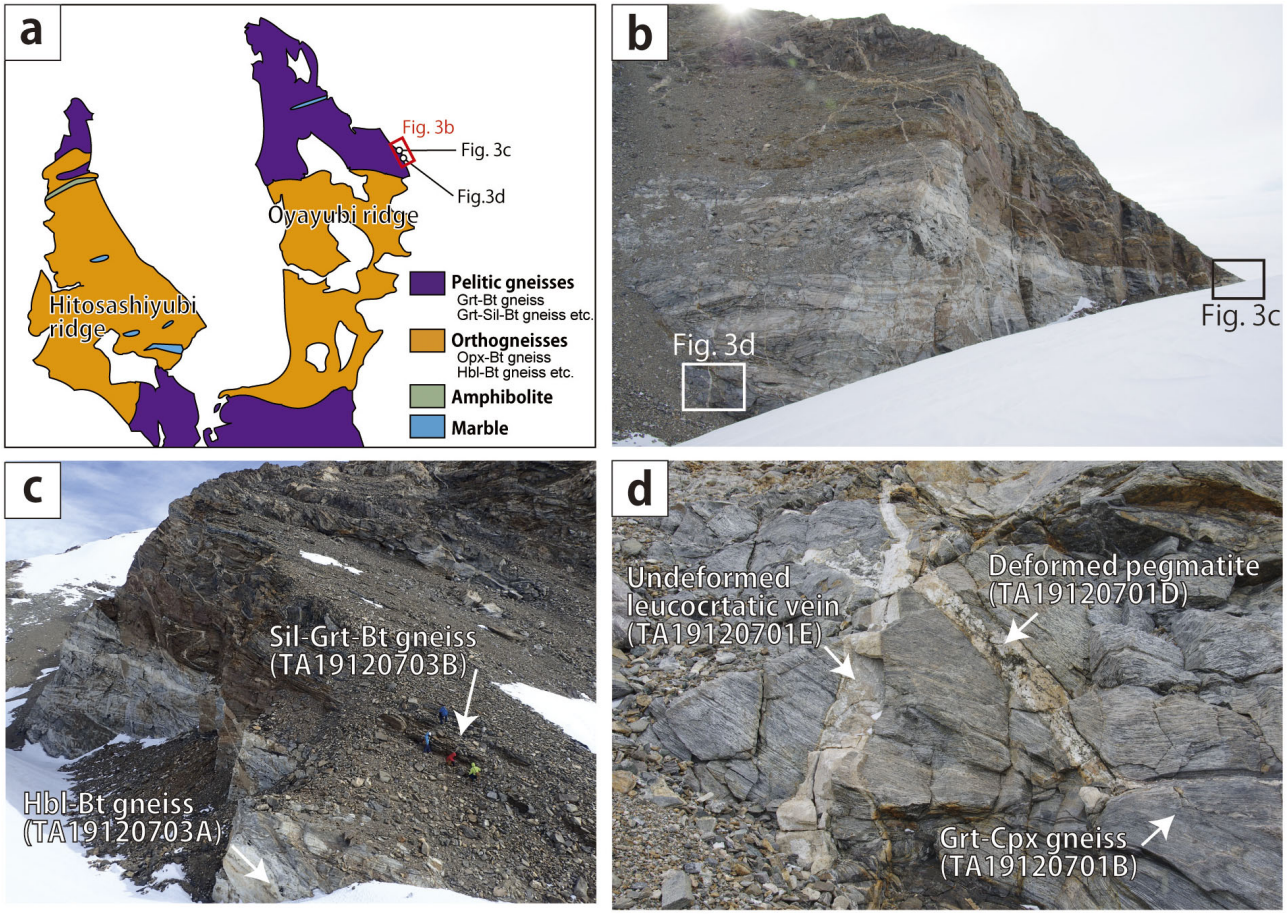

Figure 3. Mode of occurrences of the studied samples. (a) Enlarged geological map of Oyayubi ridge (modified after Osanai et al., 1996). Orthogneisses (Opx-Bt gneiss, Hbl-Bt gneiss, etc.) shown in the southern part of Oyayubi ridge are a series of structurally upper pelitic gneiss in this study. Those orthogneisses are different from structurally lower orthogneisses in this study. The structurally lower orthogneisses at Oyayubi ridge are not represented on the geological map. (b) Field photo of the outcrop at eastern slope of Oyayubi ridge. Brownish rocks at the structurally upper part are pelitic gneisses and grayish rocks at the lower part are orthogneisses. (c) Field relationship between sillimanite–garnet–biotite gneiss (TA19120703B) and hornblende–biotite gneiss (TA19120703A). (d) Feld relationship between garnet–clinopyroxene gneiss (TA19120701B), deformed pegmatite (TA19120701D) and undeformed leucocratic vein (TA19120701E). Undeformed leucocratic vein cuts all other lithologies.

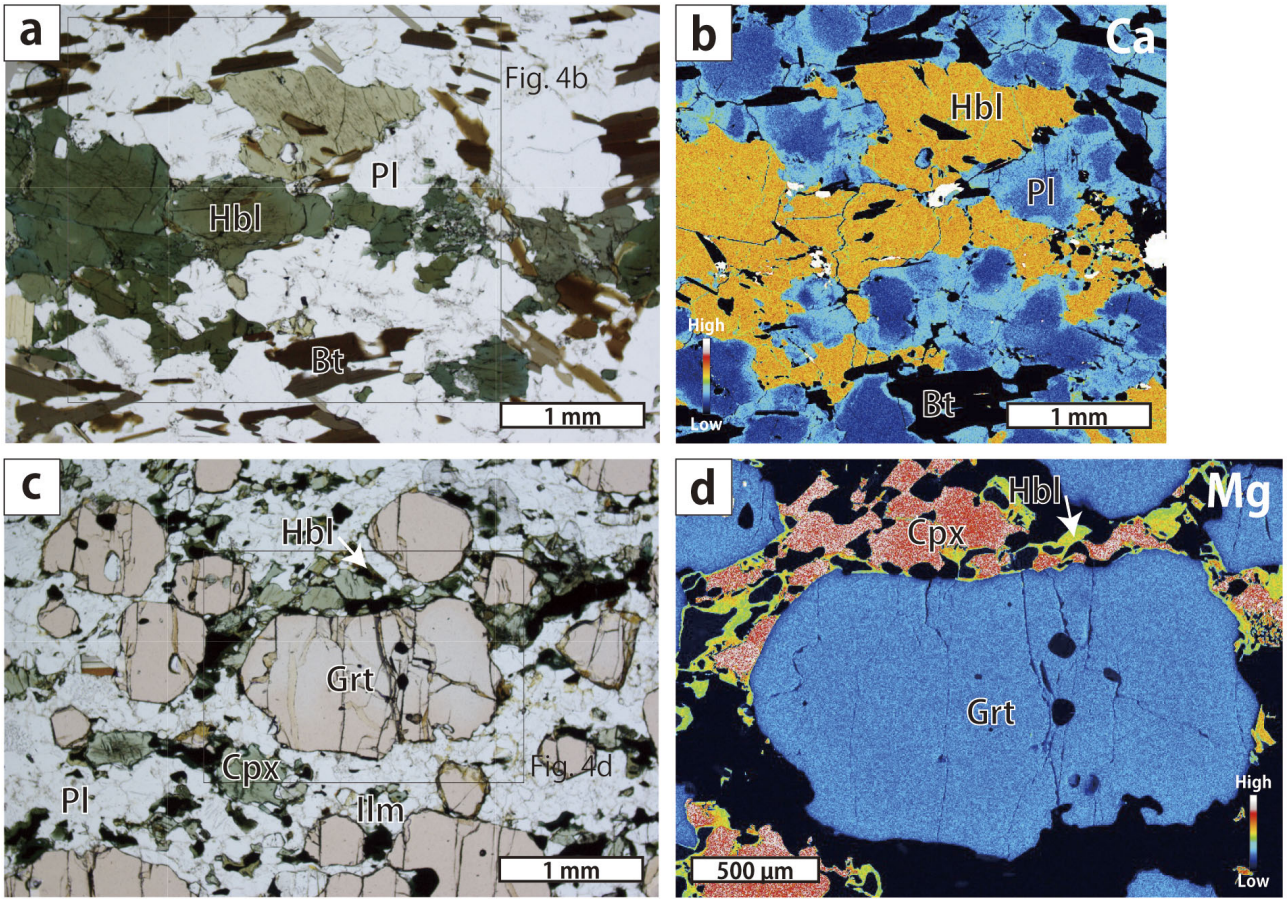

Figure 4. Photomicrographs and X-ray elemental maps of hornblende-biotite gneiss (TA19120703A) and garnet-clinopyroxene gneiss (TA19120701A). (a) Mineral assemblage in the matrix of the hornblende-biotite gneiss. (b) X-ray elemental map of calcium for the hornblende-biotite gneiss. Hornblende is mostly homogeneous, but plagioclase shows clear calcium increase at the rim. (c) Mineral assemblage in the matrix of the garnet-clinopyroxene gneiss. (d) X-ray elemental map of magnesium for the garnet-clinopyroxene gneiss. Most minerals are chemically homogeneous in this rock.

Hornblende-biotite gneiss

The hornblende-biotite gneiss (sample TA19120703A) consists of hornblende, biotite, plagioclase, quartz, and ilmenite along with minor apatite and zircon. Titanite, epidote, and chlorite are present as secondary minerals (Fig. 4a).

The hornblende and biotite grains have a preferred orientation that defines the foliation. The hornblendes in this sample are chemically homogeneous [X_{Mg} = 0.52–0.56, $(Na + K)_A$ = 0.57–0.74] except for a few rim portions or along cracks [X_{Mg} = 0.56–0.60, $(Na + K)_A$ = 0.44–0.71] (Figs. 7a and 7b). A few grains are replaced by titanite, epidote, and chlorite. The biotites are also chemically homogeneous (X_{Mg} = 0.53–0.59, TiO_2 = 1.51–2.99 wt%, Cl = 0.22–0.31 wt%) (Figs. 7c and 7d). Some biotite grains are replaced by chlorite along the cleavage. The plagioclases show clear chemical zoning with lower An contents at the cores (An_{34-45}) and higher contents at the rims (An_{40-47}) (Figs. 4b and 7f). Zircon is present in the matrix.

Garnet-clinopyroxene gneiss

The garnet-clinopyroxene gneiss (sample TA19120701B) consists of clinopyroxene, garnet, hornblende, plagioclase, quartz, and ilmenite along with minor apatite and zircon (Fig. 4c).

The garnets enclose grains of clinopyroxene, and vice versa. The garnets ($Alm_{67}Sps_1Prp_9Grs_{23}$) and clinopyroxenes ($X_{Mg}$ = 0.45–0.49) have mostly homogeneous chemical compositions (Figs. 4d, 7e, and 7g). Hornblende [(X_{Mg} = 0.26–0.31, $(Na + K)_A$ = 0.68–0.80)] (Figs. 7a and 7b) commonly surrounds clinopyroxene and ilmenite, and it is never included in garnet or clinopyroxene. The matrix plagioclase has mostly a homogeneous chemical composition (An_{27-32}), but several grains show antiperthitic textures in the host plagioclase (An_{27-31}) with K-feldspar lamellae (Ab_{4-8}) (Fig. 7f). Zircon is present in the matrix as

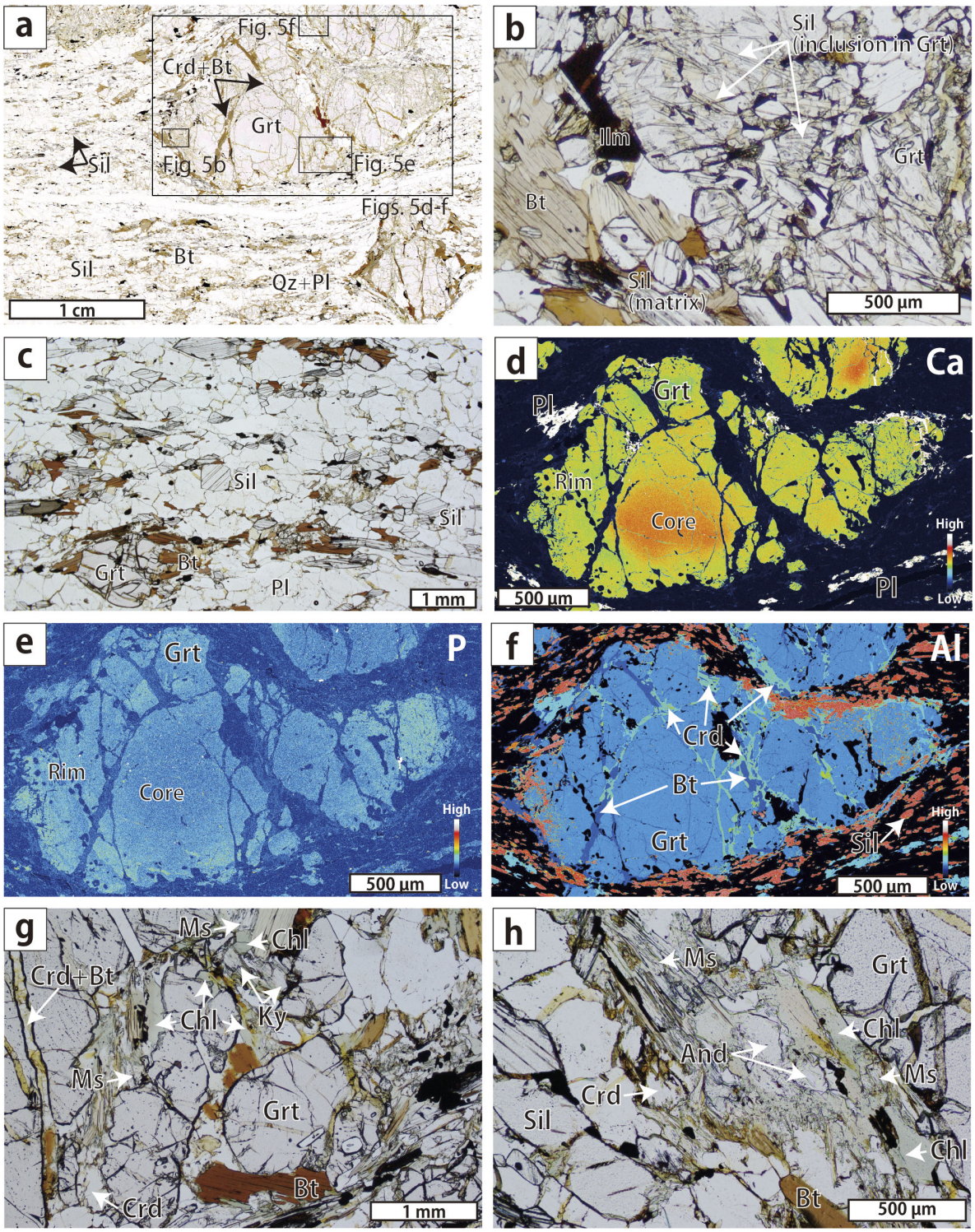

Figure 5. Photomicrograph of sillimanite-garnet-biotite gneiss (TA19120703B). (a) Mineral assemblage in the matrix of the sillimanite-garnet-biotite gneiss. A huge garnet porphyroblast is elongated. Biotite and sillimanite define foliation of this rock. Note that sillimanite is randomly oriented on the foliation plane. (b) Thin sillimanite included in the rim of the garnet. (c) Mode of occurrence of biotite and prismatic sillimanite in the matrix. (d) X-ray elemental map of calcium in the garnet. The core of the garnet preserves slightly higher calcium contents than the rim. (e) X-ray elemental map of phosphorus in the garnet. The rim of the garnet shows slightly higher phosphorus contents than the core. (f) X-ray elemental map of aluminum showing the mode of occurrence of the cordierite and biotite replacing the garnet along the crack that is oblique to the foliation plane defined by sillimanite. Garnet is shown in light blue, cordierite in light green, biotite in blue and sillimanite in red in this elemental map. (g) and (h) Modes of occurrence of the chlorite and muscovite replacing the cordierite and biotite. (g) Kyanite associated with the chlorite and muscovite. (h) Andalusite associated with the chlorite and muscovite.

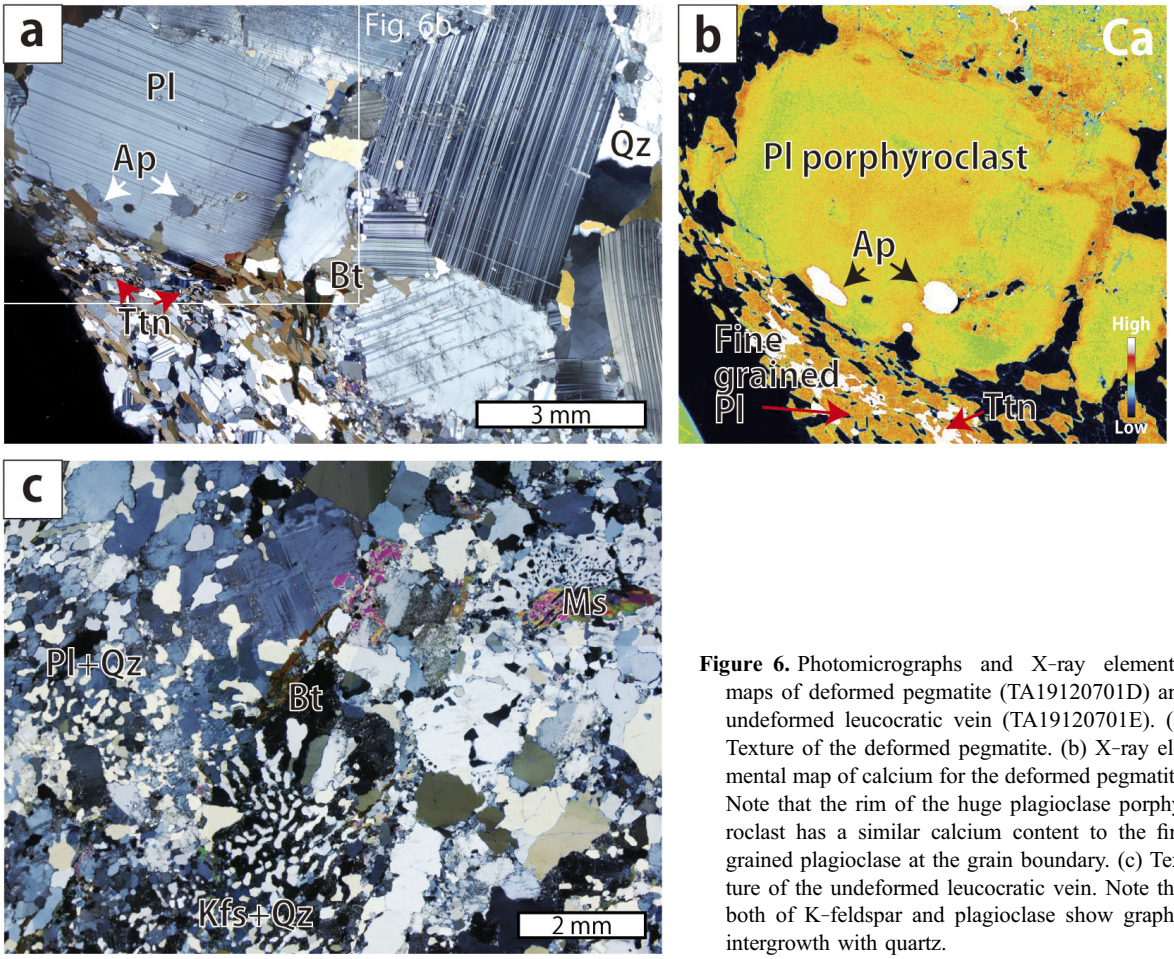

Figure 6. Photomicrographs and X-ray elemental maps of deformed pegmatite (TA19120701D) and undeformed leucocratic vein (TA19120701E). (a) Texture of the deformed pegmatite. (b) X-ray elemental map of calcium for the deformed pegmatite. Note that the rim of the huge plagioclase porphyroclast has a similar calcium content to the fine grained plagioclase at the grain boundary. (c) Texture of the undeformed leucocratic vein. Note that both of K-feldspar and plagioclase show graphic intergrowth with quartz.

well as completely or partially included in garnet.

Sillimanite-garnet-biotite gneiss

The sillimanite-garnet-biotite gneiss (sample TA1912 0703B) consists mainly of biotite, garnet, sillimanite, plagioclase, and quartz along with minor amounts of ilmenite, rutile, apatite, zircon, monazite, and xenotime (Figs. 5a and 5c). Cordierite is present along cracks in the garnets (Fig. 5f). Muscovite, chlorite, kyanite, and andalusite occur as secondary minerals (Figs. 5g and 5h).

Sillimanite occurs in the matrix, in garnet and in cordierite. The sillimanite in the matrix (Fe_2O_3 = ~ 0.4 wt%) is randomly oriented on the foliation planes and is clearly coarser than that enclosed in garnet or cordierite (Fig. 5c). Several grains in the matrix include zircon. Biotite is present in the matrix and fills cracks in garnet along with the cordierite. A few grains of biotite replace rims of garnet. The biotite in the matrix (X_{Mg} = 0.46-0.55, TiO_2 = 1.29-1.91 wt%, Cl = 0.70-0.80 wt%) defines the foliation. The grains replacing rims of garnet have similar chemical compositions, but with slightly lower values of X_{Mg} (X_{Mg} = 0.47-0.50, TiO_2 = 1.51-1.64 wt%, Cl = 0.69-0.76 wt%). The grains that coexist with cordierite have lower Cl contents (X_{Mg} = 0.47-0.57, TiO_2 = 1.19-2.22 wt%, Cl = 0.50-0.74 wt%) (Figs. 7c and 7d). Garnets occur as porphyroblasts, and they show mostly homogeneous chemical compositions, but the values of X_{Mg} drop in narrow areas next to cracks and grain boundaries (Fig. 7e). A slight chemical zoning defines the cores and rims of the garnets, with relatively high Ca and Y and low P in the cores, and vice versa in the rims (Figs. 5d and 5e). The cores of the garnets ($Alm_{65}Pyp_{28}Grs_6Sps_1$) include tiny grains of quartz, rutile, and monazite that have a distribution suggesting textural sector zoning of the host garnet. The garnet rims ($Alm_{66}Pyp_{29}Grs_4Sps_1$) contain fine-grained sillimanite (Fe_2O_3 = ~ 1.4 wt%), biotite (X_{Mg} = 0.65, TiO_2 = 0.29 wt%, Cl = 0.51 wt%), ilmenite, rutile (Zr < 2380 ppm), and zircon (Fig. 5b). P concentrations are heterogeneous in the rims with the outermost parts that contain fine-grained sillimanite showing high P concentrations (Fig. 5e). Rutile is also present in the matrix (Zr < 1750 ppm) (Fig. 7i). Plagioclase (An_{30-39}) and quartz are ubiquitous in the matrix. Cordierite (X_{Mg} =

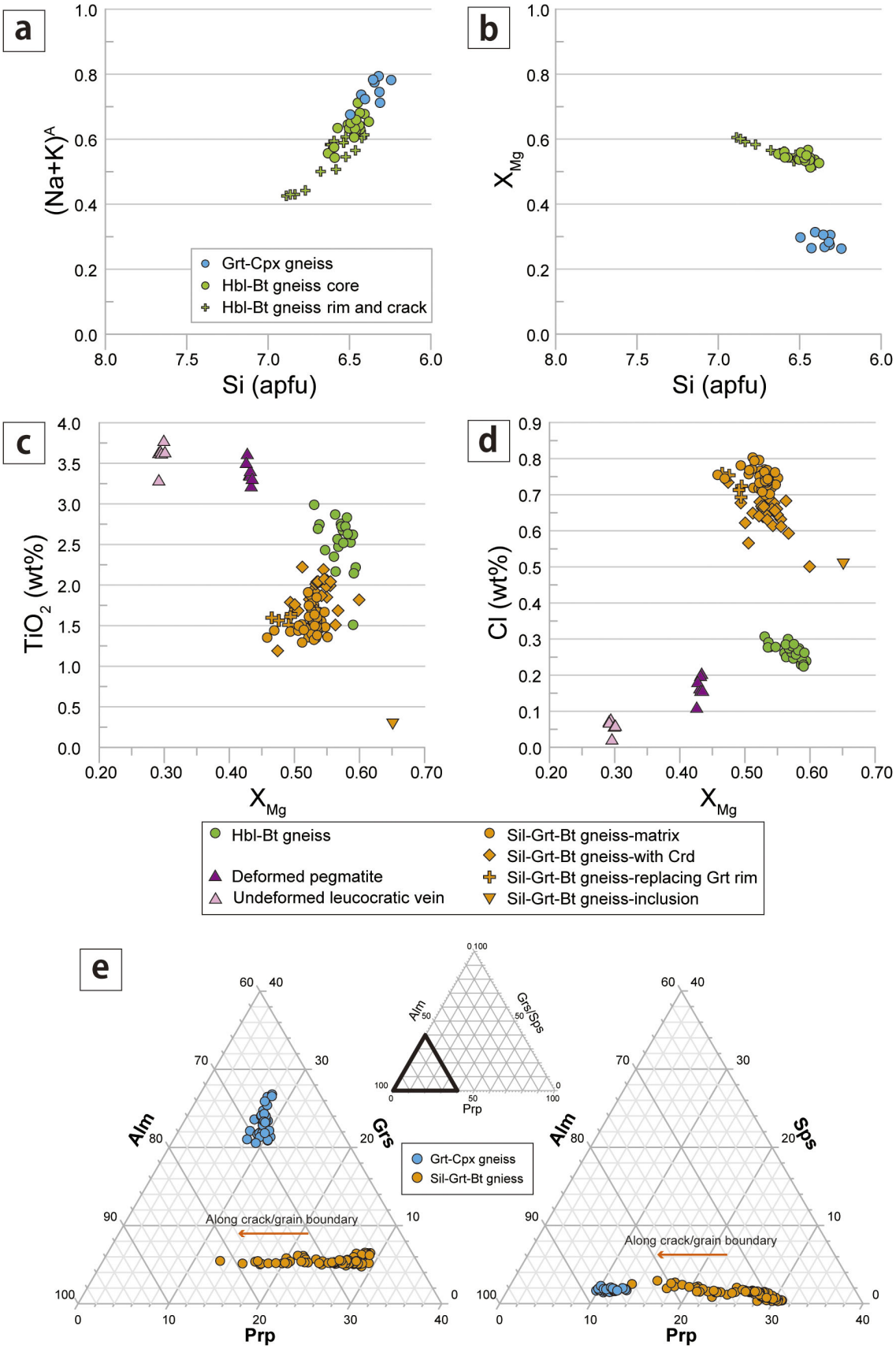
a
(Na+K)^A
Si (apfu)
Grt-Cpx gneiss
Hbl-Bt gneiss core
Hbl-Bt gneiss rim and crack
b
X_Mg
Si (apfu)
c
TiO2 (wt%)
X_Mg
d
Cl (wt%)
X_Mg
Hbl-Bt gneiss
Deformed pegmatite
Undeformed leucocratic vein
Sil-Grt-Bt gneiss-matrix
Sil-Grt-Bt gneiss-with Crd
Sil-Grt-Bt gneiss-replacing Grt rim
Sil-Grt-Bt gneiss-inclusion
e
Alm
Grs
Prp
Sps
Grs/Sps
Grt-Cpx gneiss
Sil-Grt-Bt gniess
Along crack/grain boundary
Along crack/grain boundary

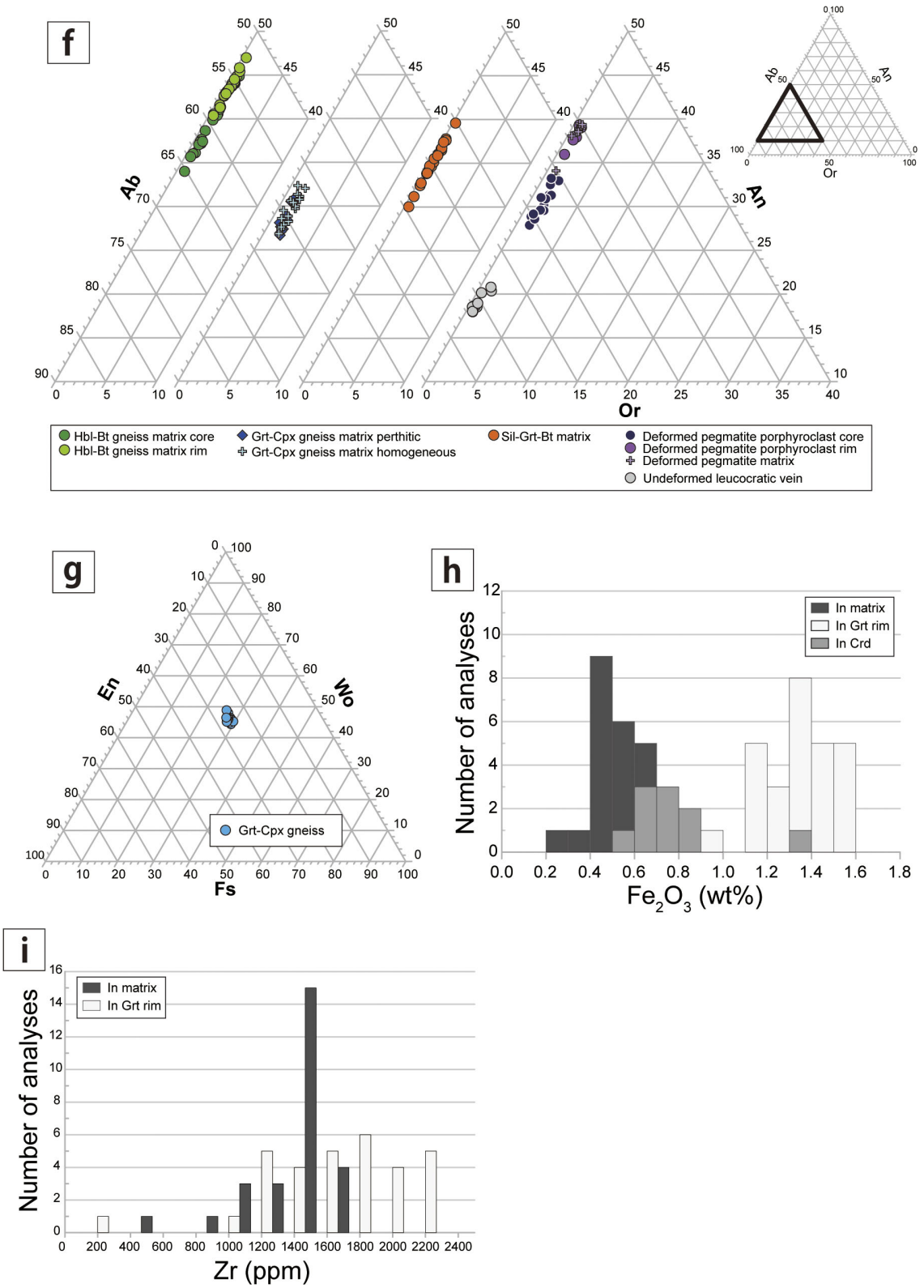

Figure 7. Diagram showing relationship between the mode of occurrences and chemical compositions of minerals in studied samples. (a) Si versus $(Na + K)_A$ diagram of hornblendes. (b) Si versus X_{Mg} diagram of hornblendes. The legend is the same as in (a). (c) X_{Mg} versus TiO_2 diagram of biotite. (d) X_{Mg} versus Cl diagram of biotite. The legend is common for (c) and (d). (e) Ternary plots for garnet. (f) Ternary plots for plagioclase. (g) Ternary plot of clinopyroxene in the Grt–Cpx gneiss. (h) Histogram of Fe_2O_3 contents (wt%) of sillimanite in Sil–Grt–Bt gneiss. (i) Histogram of Zr contents (ppm) of rutile in Sil–Grt–Bt gneiss.

~ 0.74) and biotite replace garnet along cracks that developed discordantly to the foliation of the gneiss (Fig. 5f). Cordierite in any single garnet grain shows simultaneous extinction under the microscope. Sillimanite (Fe_2O_3 = ~ 0.8 wt%) (Fig. 7h), ilmenite, zircon, and xenotime are enclosed in the cordierite and biotite. Cordierite and biotite are partly replaced by chlorite and muscovite (Figs. 5g and 5h). Kyanite and andalusite are only found with chlorite and muscovite (Figs. 5g and 5h).

Deformed pegmatite

The deformed pegmatite (sample TA19120701D) consists mainly of plagioclase, quartz, and biotite along with minor ilmenite, titanite, allanite, zircon, graphite, and apatite (Fig. 6a).

The plagioclase grains are subhedral and up to 1 cm in diameter. The thin rims of coarse grains have higher An contents ($An_{36–39}$) than the cores ($An_{28–33}$) (Figs. 6b and 7f). Finer-grained plagioclases form polygonal aggregates at grain boundaries, exhibiting a mortar texture. The finer grains have An contents ($An_{34–39}$) that are similar to those of the thin rims of the coarser subhedral plagioclases (Fig. 6b). Quartz commonly shows wavy extinction. Biotite (X_{Mg} = 0.43–0.44, TiO_2 = 3.22–3.62 wt%, Cl = 0.11–0.20 wt%) (Figs. 7c and 7d) is only weakly oriented, but it defines the foliation. Zircons occur in the matrix and are rounded.

Undeformed leucocratic vein

The undeformed leucocratic vein (sample TA19120701E) contains K-feldspar, plagioclase, and quartz along with minor biotite, apatite, allanite, and zircon (Fig. 6c).

The K-feldspars ($Ab_{4–7}Or_{96–93}$) and plagioclases ($An_{18–21}$) (Fig. 7f) in this rock both show graphic intergrowths with quartz. Randomly oriented biotite (X_{Mg} = 0.29–0.30, TiO_2 = 3.30–3.78 wt%, Cl = 0.02–0.08 wt%) (Figs. 7c and 7d) is present sporadically in the matrix. Euhedral zircon occurs in the matrix.

LA-ICP-MS U-Pb ZIRCON DATING

To determine the timing of metamorphic and igneous events, LA-ICP-MS U-Pb dating was performed on separated or in situ zircon grains. For the samples containing garnet, C1 chondrite (McDonough and Sun, 1995) normalized Yb/Gd ratios (Yb_n/Gd_n) were determined to give an indication of whether the analyzed domains coexisted with garnet. Errors on individual spot ratios and dates are quoted at 2σ, and weighted mean ^{206}Pb–^{238}U ages, calculated using concordant dates (discordance between −5% and 5%), are quoted at the 95% confidence level. Summaries of the results are given in Tables S3 and S4.

Hornblende-biotite gneiss

Zircons in the hornblende-biotite gneiss (sample TA19120703A) have oval shapes and short diameters of 80–150 μm. The core domains preserve oscillatory zoning, surrounded by vaguely zoned rim domains (Fig. 8a). The concordant dates for the cores are scattered between 614 and 518 Ma, but their distribution can be unmixed into two components (600 ± 15 Ma and 550 ± 12 Ma). The younger of these clusters is coeval with the weighted mean ^{206}Pb–^{238}U age of the rims (551 ± 8 Ma, n = 9, mean square of weighted deviation (MSWD) = 1.0) (Fig. 9a). The Th/U ratios of the cores vary from 0.12 to 0.62, whereas those of the rims show a narrower range and relatively lower values (0.06–0.25; Fig. 9b).

Garnet-clinopyroxene gneiss

Zircons in the garnet-clinopyroxene gneiss (sample TA19120701B) have oval shapes and short diameters of 100–150 μm. The grains consist of three domains: oscillatory-zoned dark CL cores, brighter CL mantles, and bright CL rims (Fig. 8b). Each domain was analyzed in situ in thin section and yielded different chemical compositions and dates (Figs. 10a–10c). The cores yielded a weighted mean ^{206}Pb–^{238}U age of 600 ± 14 Ma (n = 9, MSWD = 2.5) with Th/U and Yb_n/Gd_n ratios of 0.33–0.68 and 9.4–21.2, respectively. The mantle domains yielded a weighted mean ^{206}Pb–^{238}U age of 573 ± 17 Ma (n = 9, MSWD = 2.9) with slightly lower Th/U (0.15–0.49) and Yb_n/Gd_n (5.2–14.5) ratios than the core domains (Figs. 10b and 10c). The rims yield a weighted mean ^{206}Pb–^{238}U age of 557 ± 9 Ma (n = 7, MSWD = 0.71), and the Th/U (0.08–0.20) and Yb_n/Gd_n (1.54–6.62) ratios are lower than those in the other domains (Figs. 10b and 10c).

Sillimanite-garnet-biotite gneiss

Zircons in the sillimanite-garnet-biotite gneiss (sample TA19120703B) occur as inclusions in sillimanite, in the rims of garnet, and in the matrix. They are rounded and have diameters of 30–100 μm. The inherited cores commonly preserve oscillatory zoning that is truncated by the vaguely zoned rims. The rims of some grains in the matrix are surrounded by outer rims that are bright in CL images (Fig. 8c).

The inherited cores (n = 15) yielded concordant dates of 1100–1000, 960–920, 870, 800–740, and 620 Ma, and they have relatively high Th/U (0.08–1.29) and Yb_n/Gd_n

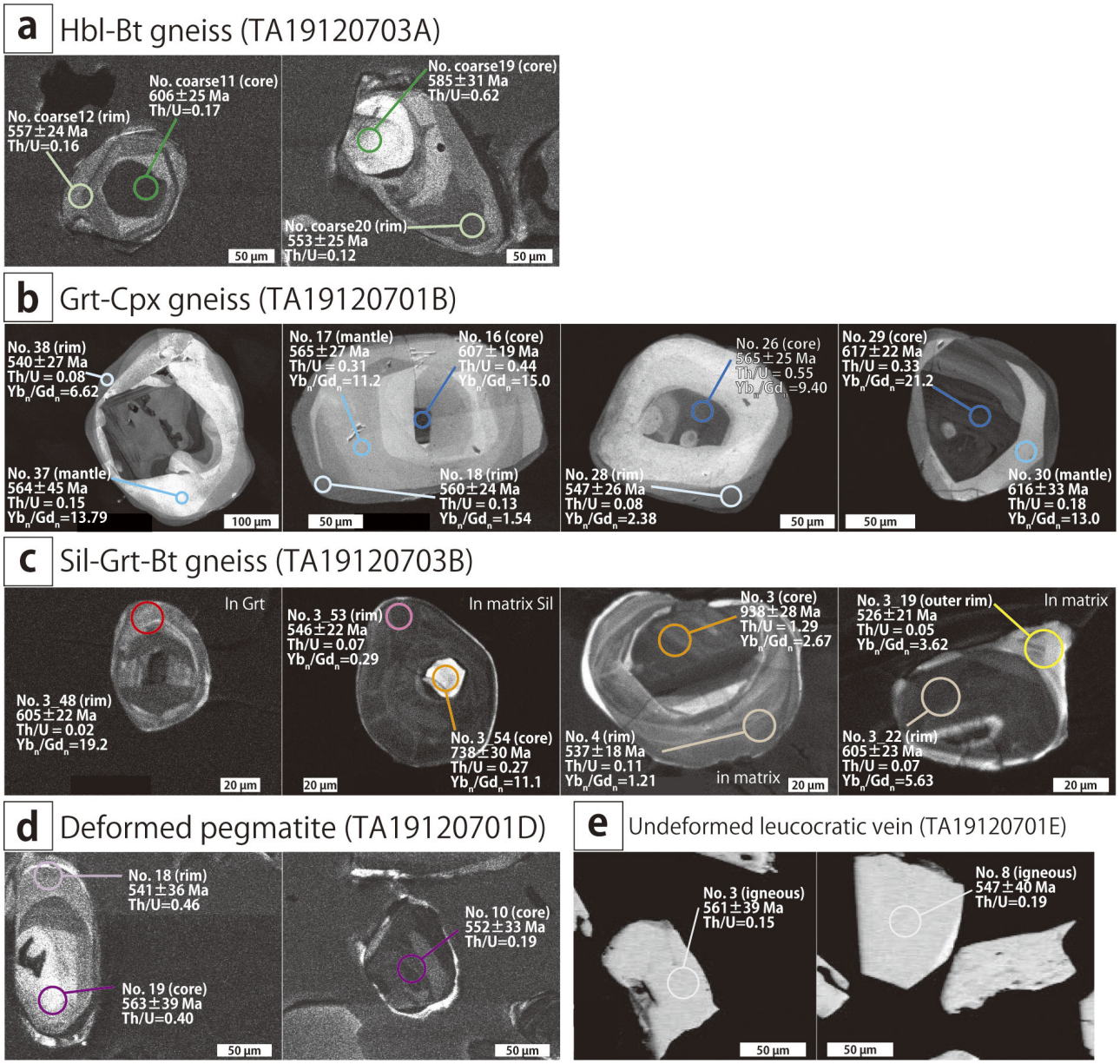

Figure 8. Representative internal textures of analyzed zircons. Analytical points are marked with circle. ^{206}Pb–^{238}U dates, Th/U ratios and Yb_n/Gd_n ratios are also shown. (a) CL images of grains of Hbl-Bt gneiss (TA19120703A). (b) CL images of grains of Grt-Cpx gneiss (TA19120701B). (c) CL images of grains of Sil-Grt-Bt gneiss (TA19120703B). (d) CL images of grains of deformed pegmatite (TA19120701D). (e) BSE images of grains of undeformed leucocratic vein (TA19120701E).

(2.67–38.71) ratios (Figs. 11a and 11b).

The dates of the vaguely zoned rims of zircon grains enclosed in garnet rims (n = 7) range between 740 and 590 Ma, but most of the dates plot around 620–590 Ma (Figs. 11c and 11d). These rims have Th/U (0.01–0.06) and Yb_n/Gd_n (1.39–21.97) ratios that are lower than those of the inherited cores (Figs. 11b and 11e). All but three dates of the rims of zircons enclosed in sillimanite (n = 11) are concentrated in a narrow range between 580 and 550 Ma with a peak at ~ 570 Ma. (Figs. 11c and 11d). The Th/U (0.02–0.15) and Yb_n/Gd_n (0.21–5.26) ratios in these rims are low, but the low Yb_n/Gd_n ratios are particularly distinctive (Figs. 11b and 11e). The dates obtained for the rims of matrix zircons show a relatively wide range of 700–530 Ma (Figs. 11c and 11d). The Th/U (0.01–0.16) and Yb_n/Gd_n (0.23–18.73) ratios are similar to those of the grains enclosed within sillimanite (Figs. 11b and 11e). One analysis of an outer rim of a matrix grain gave an age of 526 ± 21 Ma with Th/U = 0.05 and Yb_n/Gd_n = 3.62 (Figs. 11a–11e).

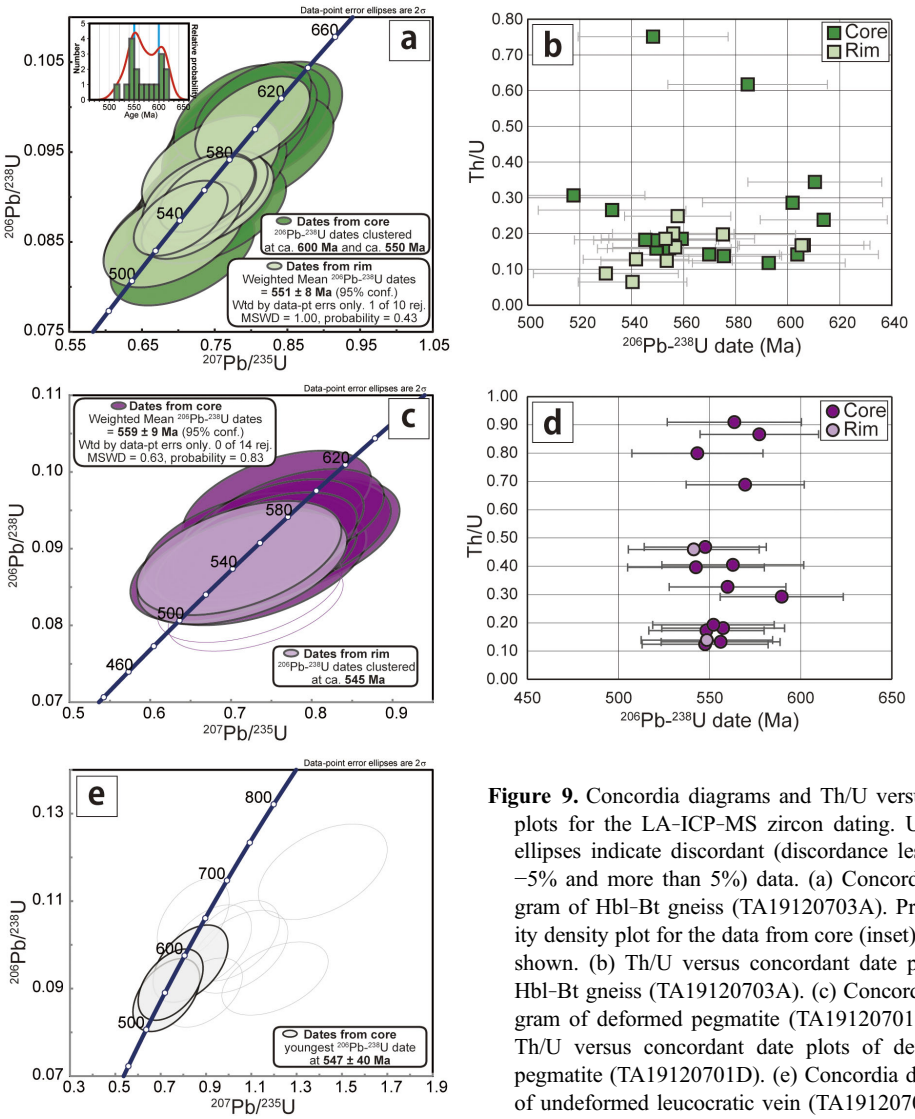

Figure 9. Concordia diagrams and Th/U versus date plots for the LA-ICP-MS zircon dating. Unfilled ellipses indicate discordant (discordance less than −5% and more than 5%) data. (a) Concordia diagram of Hbl-Bt gneiss (TA19120703A). Probability density plot for the data from core (inset) is also shown. (b) Th/U versus concordant date plots of Hbl-Bt gneiss (TA19120703A). (c) Concordia diagram of deformed pegmatite (TA19120701D). (d) Th/U versus concordant date plots of deformed pegmatite (TA19120701D). (e) Concordia diagram of undeformed leucocratic vein (TA19120701E).

Deformed pegmatite

Zircons in the deformed pegmatite (sample TA19120701D) are oval in shape with short diameters of 50–100 μm. The oscillatory zoning in the cores of these grains is truncated by vaguely zoned rim domains (Fig. 8d). Most of the data were obtained from the core domains, which yield a weighted mean ^{206}Pb–^{238}U age of 559 ± 9 Ma (n = 14, MSWD = 0.63) with Th/U = 0.12–0.91. Two analyses of rims indicate slightly younger dates (541 and 547 Ma; Figs. 9c and 9d).

Undeformed leucocratic vein

Zircons in the undeformed leucocratic vein (sample TA19120701E) are euhedral and prismatic in shape with short diameters of 30–50 μm. The grains show extremely low CL emissions and their internal texture is unclear (Fig. 8e). The dates are scattered on a concordia diagram, but we obtained a youngest concordant date of 547 ± 40 Ma (Fig. 9e).

DISCUSSION

Pressure-temperature conditions of the rocks from Oyayubi ridge

The metamorphic rocks in the SRM commonly affected by intense retrograde hydration that makes it difficult to estimate prograde-peak metamorphic conditions (e.g., Adachi et al., 2010). However, our samples show only limited evidence of retrograde hydration, and we tried, therefore, to estimate the metamorphic *P*–*T* conditions of these samples.

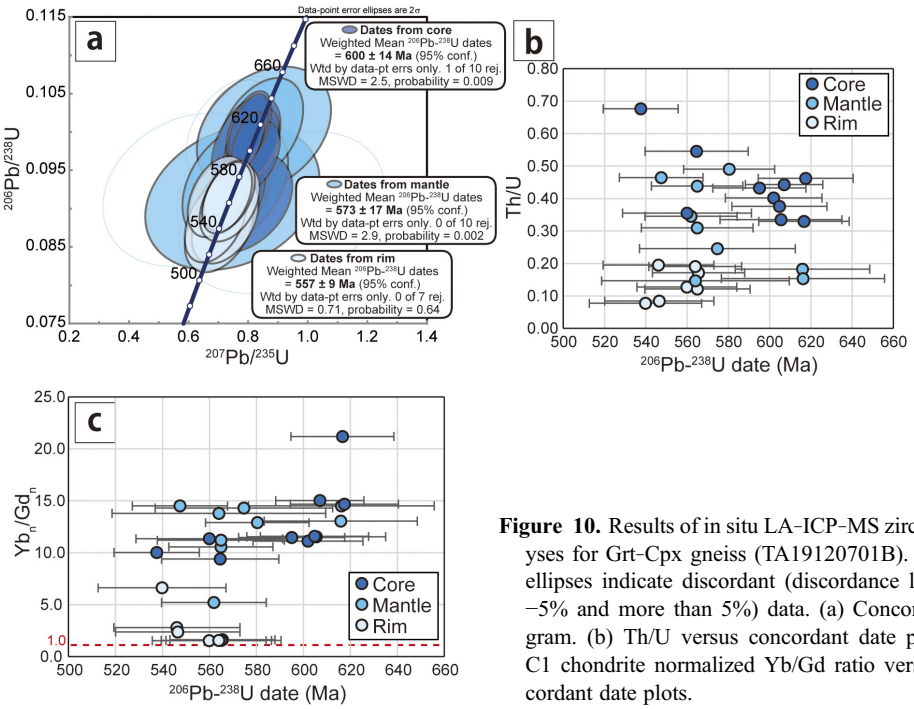

Figure 10. Results of in situ LA-ICP-MS zircon analyses for Grt-Cpx gneiss (TA19120701B). Unfilled ellipses indicate discordant (discordance less than −5% and more than 5%) data. (a) Concordia diagram. (b) Th/U versus concordant date plots. (c) C1 chondrite normalized Yb/Gd ratio versus concordant date plots.

Hornblende-biotite gneiss. The hornblendes in this rock have almost homogeneous compositions except for a few rim portions or along cracks, and therefore the grains mostly preserve the original compositions that were obtained under peak metamorphic conditions. The plagioclases show obvious chemical zoning such as a rimward increase in An content (Fig. 4b), and the rims probably equilibrated with the hornblendes under peak metamorphic conditions. The peak metamorphic conditions may, therefore, be estimated using the chemical compositions of the homogeneous cores of the hornblendes and the rims of the plagioclases. The hornblende-plagioclase geothermometer (Holland and Blundy, 1994) and hornblende-plagioclase-quartz geobarometer (Bhadra and Bhattacharya, 2007) gave 698-750 °C and 0.57-0.91 GPa (Fig. 12a).

Garnet-clinopyroxene gneiss. Since we found no evidence of retrograde metamorphism, the minerals in the matrix of this gneiss can be interpreted to have equilibrated under the peak metamorphic conditions. Chemically homogeneous garnet, clinopyroxene, and plagioclase may be used for peak *P-T* estimates using the garnet-clinopyroxene geothermometer (Nakamura, 2009) and the garnet-clinopyroxene-plagioclase-quartz geobarometer (Newton and Perkins, 1982), and they gave *P-T* conditions of 694-765 °C and 0.54-0.73 GPa (Fig. 12a).

Sillimanite-garnet-biotite gneiss. The porphyroblasts of garnet are almost chemically homogeneous except for their Ca, Y, and P contents. The slight heterogeneities define core and rim domains in the garnets. The cores show textural sector zoning, suggesting relatively rapid growth during prograde metamorphism. The presence of sillimanite as inclusions in garnet rims and as a matrix phase indicates that the prograde and peak *P-T* conditions were in the stability field of sillimanite.

The replacement of garnet porphyroblasts by cordierite + biotite along cracks oblique to the foliation in the matrix (Fig. 5f) suggest that the following reaction occurred after the main deformation of the rock:

$$\mathrm{Grt} + \mathrm{Kfs} + \mathrm{melt} \rightarrow \mathrm{Crd} + \mathrm{Bt} + \mathrm{Qz} \quad (1).$$

This reaction would have taken place in the sillimanite stability field, as sillimanite is present in the cordierite. The absence of K-feldspar in this rock may indicate that it was consumed by this reaction. Although there is no direct evidence for the existence of a melt, given the *P-T* conditions of the peak metamorphism described below, it is probable that melts were present during/after the peak metamorphism.

Cordierite and biotite are replaced by chlorite and muscovite where cracks filled by the former minerals meet the matrix (Figs. 5g and 5h), which suggests the following hydration reaction:

$$\mathrm{Crd} + \mathrm{Bt} + \mathrm{H_2O} \rightarrow \mathrm{Chl} + \mathrm{Ms} \quad (2).$$

Kyanite and andalusite are found only in association with this chlorite and muscovite (Figs. 5g and 5h), which in-

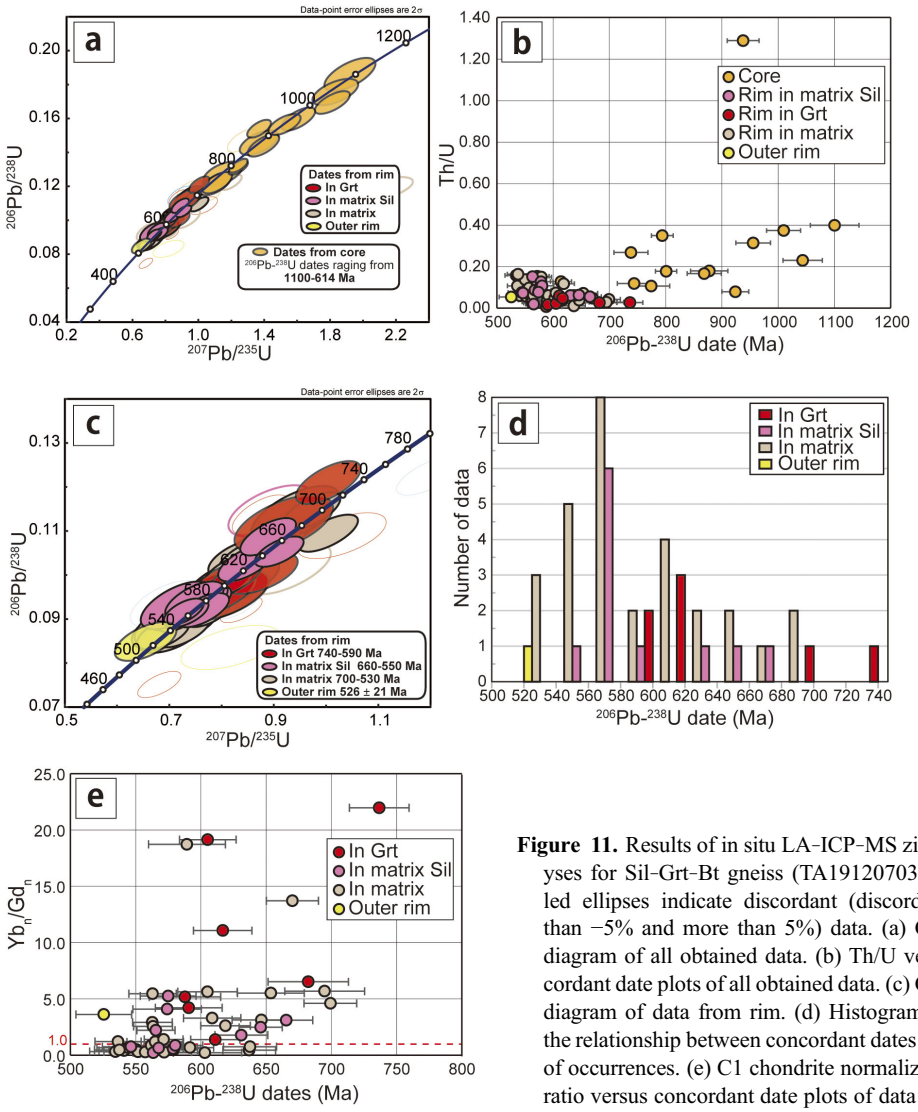

Figure 11. Results of in situ LA-ICP-MS zircon analyses for Sil-Grt-Bt gneiss (TA19120703B). Unfilled ellipses indicate discordant (discordance less than −5% and more than 5%) data. (a) Concordia diagram of all obtained data. (b) Th/U versus concordant date plots of all obtained data. (c) Concordia diagram of data from rim. (d) Histogram showing the relationship between concordant dates and mode of occurrences. (e) C1 chondrite normalized Yb/Gd ratio versus concordant date plots of data from rim.

dicates the following reaction:

$$\text{Sil} \rightarrow \text{Ky/And} \qquad (3),$$

which probably occurred at the same time as reaction (2). If that were the case, reaction (2) would have occurred around the *P*–*T* conditions for kyanite and andalusite transition.

Biotite has four modes of occurrence in the sillimanite-garnet-biotite gneiss: in the matrix, along cracks in garnet with cordierite, replacing garnet rims, and as inclusions in garnet. Biotite in each mode is compositionally distinct (Figs. 7c and 7d) and can be interpreted in terms of being in equilibration with adjacent minerals. Plagioclase is only found in the matrix of this rock, and it has only a small range of An values (Fig. 7f). The garnets show almost homogeneous chemical compositions except for narrow areas next to cracks and grain boundaries (Fig. 7e). This suggests there was little chemical modification after equilibrium was reached with the matrix minerals. Based on these observations, *P*–*T* conditions around the peak condition can be estimated using garnet rims, away from cracks and grain boundaries, biotites in the matrix, and plagioclases in the matrix. The combination of the garnet-biotite geothermometer (Holdaway, 2000) and the garnet-aluminosilicate-plagioclase-quartz (GASP) geobarometer (Holdaway, 2001) yielded *P*–*T* conditions of ~ 732–824 °C and 0.66–0.86 GPa (Fig. 12b). The temperature estimate is consistent with the results obtained by applying the Zr-in-rutile thermometer (Tomkins et al., 2007) to rutile in the matrix (<801 °C, average 775 °C) assuming a pressure of 0.8 GPa. A slightly higher temperature (<837 °C, average 802 °C, at a pressure of 0.8 GPa) was obtained for rutile in the garnet rims, which probably indicates the peak temperature. When combined with the

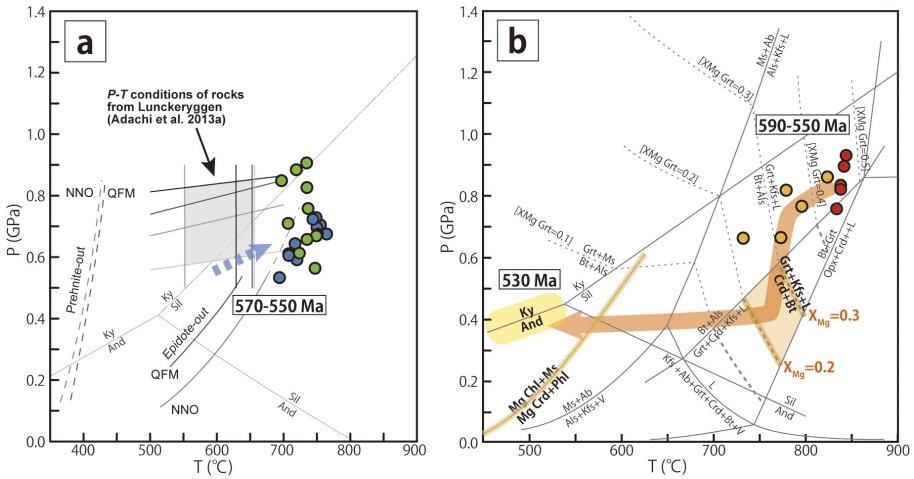

Figure 12. Estimated *P–T* conditions of the studied samples. (a) Estimated *P–T* conditions of the Grt–Cpx gneiss and Hbl–Bt gneiss. Peak *P–T* conditions are estimated using Grt–Cpx geothermometer (Nakamura, 2009) and Grt–Cpx–Pl–Qz geobarometer (Newton and Perkins, 1982) for Grt–Cpx gneiss (blue filled circles) and Hbl–Pl geothermometer (Holland and Blundy, 1994) and Hbl–Pl–Qz geobarometer (Bhadra and Bhattacharya, 2007) for Hbl–Bt gneiss (green filled circles), respectively. *P–T* conditions of gneisses from Lunckeryggen (Adachi et al., 2013b) are also shown. Prehnite and epidote–out reaction curves are after Liou (1973) and Liou et al. (1983). (b) Estimated *P–T* path of the Sil–Grt–Bt gneiss. Petrogenetic grid for the NaKFMASH system with contours of Mg/(Fe + Mg) = 0.1–0.5 in garnet are from Spear et al. (1999). *P–T* conditions (red and orange filled circles) are estimated using Zr in rutile geothermometer (Tomkins et al., 2007) and Grt–Bt geothermometer (Holdaway, 2000), respectively, combined with GASP geobarometer (Holdaway, 2001).

GASP geobarometer (Holdaway, 2001), the chemical compositions of rutile in the garnet rims, the rims of the garnet, and the plagioclase in the matrix yielded *P–T* conditions of 834–844 °C and 0.76–0.93 GPa, which can be interpreted to reflect the peak metamorphism. The slightly lower temperature estimates for minerals in the matrix might indicate re-equilibration during cooling.

The pressure and temperature conditions of reaction (1) for the observed garnet and cordierite compositions of X_{Fe}^{Grt} = 0.69–0.74 and X_{Mg}^{Crd} = 0.72–0.78 are inferred to be ~ 750–800 °C and 0.2–0.6 GPa in the NaKFMASH system (Spear et al., 1999) (Fig. 12b). These conditions are similar to the temperature but lower than the pressure conditions of the peak metamorphism. Therefore, reaction (1) in this sample would have taken place accompanied by isothermal decompression after the peak metamorphism.

Since the cordierite, biotite, and chlorite in this rock are Fe–Mg solid solutions, reaction (2) for this sample took place at lower temperatures than for the Mg end-member minerals (Spear et al., 1999). In addition, kyanite and andalusite are found associated exclusively with chlorite and muscovite. Therefore, we suggest that reaction (2) in this rock occurred around the *P–T* conditions for kyanite/andalusite transition; i.e., at least under lower temperature and pressure conditions than the Al_2SiO_5 triple point (530 °C, 0.4 GPa; Bohlen et al., 1991) (Fig. 12b).

Consequently, we propose that the *P–T* path of the cordierite–bearing sillimanite–garnet–biotite gneiss records the peak metamorphism at ~ 830–840 °C and 0.8–0.9 GPa, a subsequent isothermal decompression, and then a retrograde hydration at *P–T* conditions lower than 530 °C and 0.4 GPa (Fig. 12b).

Undeformed leucocratic vein. The plagioclase and K–feldspar in this rock are chemically homogeneous, and we used their compositions to estimate the temperatures of crystallization using the two–feldspar thermometer (Fuhrman and Lindsley, 1988). The geothermometer gave *P–T* conditions of ~ 390–440 °C assuming 0.2–1.0 GPa, with little dependence on pressure. These temperatures are much lower than the solidus of the granite system (Johannes, 1984), and they are therefore interpreted as temperatures of subsolidus recrystallization.

Correspondence between *P–T* conditions and zircon U–Pb ages

The rims of zircons in the hornblende–biotite gneiss yielded an age of 551 ± 8 Ma, interpreted as the timing of the metamorphism, based on the low Th/U ratios and vague zoning in these zircon rims. The oscillatory zoning in the cores of these grains indicates their igneous origin, and they yielded ages of 600 ± 15 Ma and 550 ± 12 Ma. The younger age of the core is coeval with the age of the rim, which implies that the younger age of the core resulted from isotopic modification during metamorphism, even though the original igneous textures are preserved. The older age should represent the igneous activity, which formed the protolith of this gneiss.

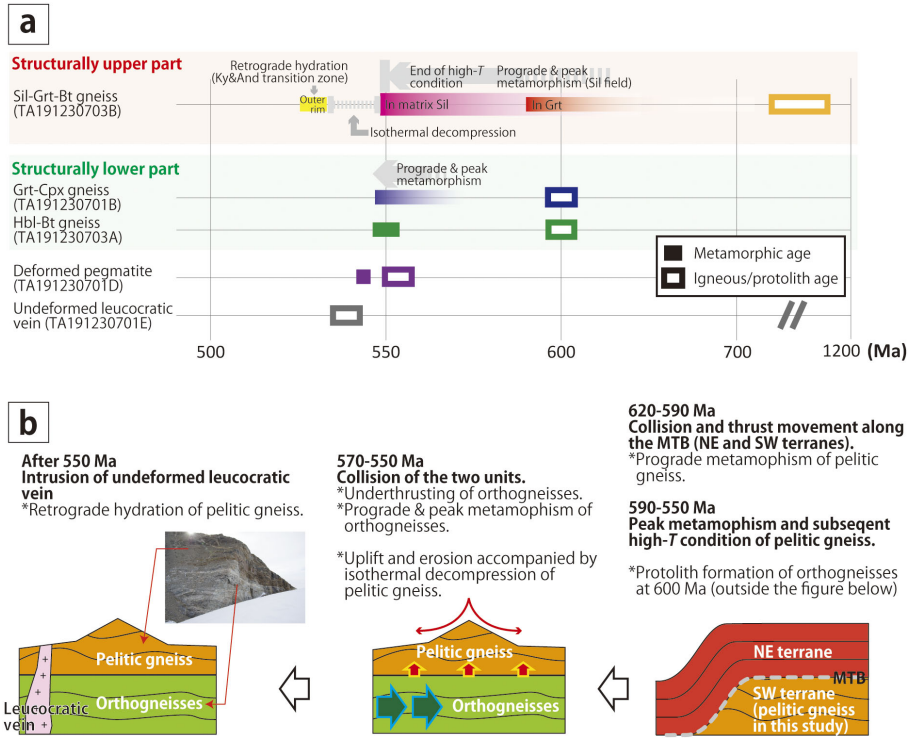

Figure 13. Summary of metamorphism and geochronology of Oyayubi ridge, Brattnipene. (a) Temporal relationship between structurally upper pelitic gneiss and lower orthogneisses. Open squares indicate igneous/protolith ages and filled squares indicate metamorphic ages. The color of squares are the same as in Figures 9-11. (b) Possible geological history based on the *P*-*T*-*t* paths of pelitic gneiss and orthogneisses.

The timing of protolith formation at ~ 600 Ma is also preserved in the garnet-clinopyroxene gneiss, where the oscillatory zoned zircon cores yielded an age of 600 ± 14 Ma. The other two ages given by zircons in the garnet-clinopyroxene gneiss (i.e., 573 ± 17 Ma for mantles and 557 ± 9 Ma for rims) are interpreted to represent the timing of metamorphism, based on their vaguely zoned textures. The rims are observed on zircon grains in both the matrix and the garnet, and this means that the garnets formed at ~ 560 Ma at the latest. Since garnet and clinopyroxene, which are the matrix minerals in this rock, contain inclusions of each other, these minerals grew mostly synchronously. This age, therefore, indicates the timing of the peak metamorphism. Mantles of zircon are thought to have been formed during the prograde metamorphism because they do not exhibit textures typical of an igneous origin. Thus, the hornblende-biotite and garnet-clinopyroxene gneisses are similar in the timing of their protolith formation and peak metamorphism. Moreover, the peak *P*-*T* conditions (700-760 °C, 0.6-0.9 GPa) are similar, and these consistencies as well as the field relationships strongly indicate that all the orthogneisses followed the same *P*-*T*-*t* path. Consequently, the history of the orthogneisses can be summarized as follows: (1) the protolith was formed by igneous activity at ~ 600 Ma, (2) prograde metamorphism took place at ~ 570 Ma and reached to the peak conditions of 700-760 °C and 0.6-0.9 GPa at ~ 560-550 Ma (Fig. 13a).

The orthogneisses are cut by the deformed pegmatite (Fig. 3c). Zircons in the deformed pegmatite yielded an age of ~ 560 Ma, and this is interpreted to represent the timing of intrusion because most of the zircons show oscillatory zoning throughout the entire grain. The mortar texture of fine-grained plagioclases (Figs. 6a and 6b) was probably formed by recrystallization during the deformation, and these fine mortar-textured grains as well as the rims of matrix grains have higher An contents than the cores of the matrix grains (Figs. 6b and 7f), indicating metamorphism that was synchronous with deformation. The metamorphism of the deformed pegmatite may have taken place at ~ 550 Ma, an age given by the rims of two zircons. These metamorphic rims, which are slightly younger than the cores, imply that they record the same metamorphism as the host orthogneisses after intrusion (Fig. 13a).

Unlike the orthogneisses, the zircons in the sillimanite-garnet-biotite gneiss record a metamorphism older than ~ 600 Ma. Most of the dates for the metamorphic domains of zircons enclosed in the garnet rims are clustered at 620-590 Ma (Figs. 11c and 11d), which is probably a record of the prograde metamorphism during which the garnet rims grew. The youngest date of 590 Ma means that garnet growth continued until this time at the latest (Fig. 13a). Since the highest temperature recorded in the sillimanite-garnet-biotite gneiss was estimated from rutile

enclosed in garnet rims, the timing of this temperature may be close to the timing of the peak metamorphism. The rims of zircons included in sillimanite show a cluster of dates from 580 to 550 Ma (Figs. 11c and 11d). The sillimanite in the matrix coexisted with the garnet rims, and therefore the metamorphic conditions under which the matrix mineral assemblage equilibrated, continued until 550 Ma. This suggests that high temperatures close to the peak metamorphic conditions lasted for about 40 million years, as estimated from the youngest dates of metamorphic zircons enclosed in the garnet rims and in the sillimanite of the matrix. Sillimanite in the matrix is clearly coarser grained than that enclosed in the garnet rims, and it is randomly oriented on the foliation planes. This could be the result of long-lasting high-temperature conditions without any uniaxial extension or shearing (Fig. 13a). Another scenario is that the 620–590 Ma metamorphism that formed the garnet rims was followed by another distinct 580–550 Ma metamorphism that formed the matrix sillimanite. This scenario is based on the two age peaks at ~ 600 and 560 Ma for zircons in the matrix, with the former age consistent with the dates of the zircons in the garnet rims and the latter age consistent with the dates of zircons enclosed in the matrix sillimanite. The temperatures of the ~ 580–550 Ma metamorphism, as estimated from the mineral assemblage in the matrix, are slightly lower than those during the metamorphism at ~ 620–590 Ma. Under these conditions, reactions such as

$$\mathrm{Grt} + \mathrm{Kfs} + \mathrm{H_2O} \rightarrow \mathrm{Sil} + \mathrm{Bt} + \mathrm{Qz} \quad (4),$$

must have occurred to form the sillimanite. However, no clear texture showing the replacement of garnet by sillimanite and biotite has been observed, and in many cases the sillimanite and biotite in the matrix are not closely associated (Fig. 5c). Therefore, rather than a scenario in which two distinct metamorphisms occurred, it is more likely that a single metamorphic event occurred, and that the high-temperature conditions continued for a long period. If traces of heating at around 550 Ma are found, it may be possible to test the scenario of two distinct metamorphic events. The decompression that induced the cordierite-forming reaction (1) is thought to have taken place after the high-temperatures until 550 Ma because the cracks filled with cordierite + biotite in the porphyroblasts of garnet are perpendicular to the foliation in the matrix (Figs. 5a and 5f). The youngest dates in this rock of ~ 530 Ma were obtained from the outer rims of zircons in the matrix (Figs. 11c and 11d). Similar dates were also obtained in the undeformed leucocratic vein (Fig. 9e). Based on two-feldspar thermometry, this leucocratic vein records conditions of subsolidus recrystallization at ~ 390–440 °C, assuming a pressure of 0.2–1.0 GPa. This suggests that the temperature of the melt was higher than these estimated temperatures when the vein intruded. These *P–T* conditions are consistent with those under which reactions (2) and (3) took place in the sillimanite–garnet–biotite gneiss, and they represent the last thermal event recorded in this gneiss. Such consistencies in the ages and temperatures imply that reactions (2) and (3) in the gneiss were driven by infiltration of fluids from the undeformed leucocratic vein at ~ 530 Ma (Fig. 13a). If this were the case, reaction (1) should have taken place between 550 Ma, the time of matrix sillimanite growth, and 530 Ma, the time when hydration reaction (2) took place.

Consequently, the history of the pelitic gneisses can be summarized as follows: (1) the prograde and subsequent peak metamorphism at ~ 830–840 °C and 0.8–0.9 GPa occurred at around 620–590 Ma, (2) these high temperatures lasted until 550 Ma, (3) isothermal decompression took place toward conditions of ~ 750–800 °C and 0.2–0.6 GPa, and (4) retrograde hydration reactions occurred at 530 Ma under *P–T* conditions lower than 530 °C and 0.4 GPa (probably ~ 400 °C) (Fig. 13a).

Implications for the tectonics of the SRM

The pelitic gneiss unit that structurally overlies the orthogneiss on the eastern slope of Oyayubi ridge (Figs. 3b and 3c) records isothermal decompression after the peak metamorphism, which means that it records a clockwise *P–T* path. Counterclockwise *P–T* paths are recorded by other gneisses from Brattnipene (Adachi et al., 2013a; Baba et al., 2013), which appears to contradict the results of our study. However, in those previous studies, the compression is thought to have occurred at ~ 600 Ma, predating the peak metamorphic *P–T* conditions. Here, we have suggested that the decompression of the pelitic gneiss took place between 550 and 530 Ma, after the peak *P–T* conditions, and therefore the clockwise path of the pelitic gneiss not a direct reason for not belonging to the SW Terrane. The peak *P–T* conditions of the pelitic gneiss (~ 830–840 °C and 0.8–0.9 GPa) are close to the previously reported *P–T* conditions of gneisses in Brattnipene (Adachi et al., 2013a; Baba et al., 2013), and the consistency in the timing and conditions of the peak metamorphism supports the idea that the pelitic gneiss can be correlated with the gneisses in the SW Terrane, even though the presence or absence of a pressure increase prior to the peak conditions needs to be verified from the surrounding lithologies.

In terms of having a protolith of igneous origin, and preserving prograde metamorphic textures and evidence of metamorphism at ~ 550 Ma, the orthogneisses that underlie the pelitic gneiss unit are similar to rocks in Lunck-

eryggen to the south of Brattnipene (Adachi et al., 2013a, 2013b). Therefore, the rocks in Lunckeryggen and the orthogneisses in Brattnipene can be considered to have been metamorphosed at ~ 550 Ma as a single geological unit. Although the timing of protolith formation is inconsistent, being ~ 1000–900 Ma for the rocks in Lunckeryggen and ~ 600 Ma for the orthogneisses in Brattnipene, they probably formed a single geological unit at ~ 550 Ma because these rocks underwent the same metamorphic event. Adachi et al. (2013b) interpreted the ~ 550 Ma metamorphism at Lunckeryggen to be one of contact metamorphism related to the intrusion of massive granitoid and syenite bodies, based on their sporadic distribution. In this type of metamorphism, it would be expected that the rocks closest to the igneous body would record the highest temperatures of metamorphism. However, the orthogneisses we studied record higher peak temperatures than the metamorphic rocks of Lunckeryggen (Adachi et al., 2013a), even though the orthogneisses are located farther from the intrusive body. This suggests that the ~ 550 Ma metamorphic rocks are unlikely to have been formed by contact metamorphism.

At the outcrops of Oyayubi ridge, the structurally upper pelitic gneisses reached peak metamorphic conditions at ~ 600 Ma, then cooled slightly, remaining in a high-temperature condition until at least ~ 550 Ma, and then underwent decompression at about 550–530 Ma. On the other hand, the structurally lower orthogneisses underwent a prograde metamorphism at ~ 570 Ma and reached peak conditions at ~ 550 Ma. This can be explained as the result of thrusting of the pelitic gneisses over the orthogneisses at ~ 570–550 Ma, causing a prograde metamorphism in the orthogneisses but a decompression in the pelitic gneisses, with uplift and subsequent rapid denudation taking place after ~ 550 Ma (Fig. 13b). On the other hand, the age data we present in this paper would suggest that the pelitic gneiss underwent two metamorphisms at ~ 600 Ma and ~ 550 Ma, and it may therefore be possible that some of the igneous bodies that were protoliths of the orthogneiss were intruded into the pelitic gneiss at ~ 600 Ma, and then metamorphosed at the same time as the pelitic gneiss at 570–550 Ma. If this were the case, the boundary between the pelitic gneiss unit and the orthogneisses is not a tectonic boundary but an intrusive contact that formed at ~ 600 Ma. To test which of these two ideas is correct, we need to consider the following: the first idea can be rejected if textures of prograde metamorphism at ~ 550 Ma or structures showing the protolith of the orthogneisses intruding the pelitic gneiss are found, while the second idea can be rejected if the deformation structures of the orthogneisses are cut by a lithological boundary. So far, no textures or structures have been found to reject the first idea. Moreover, it is reported that ~ 550 Ma metamorphic rocks without ~ 600 Ma metamorphic ages structurally underlie the ~ 600 Ma metamorphic rocks in other areas (Adachi et al., 2013b; Tsukada et al., 2017). We suggest, therefore, that at present, the thrusting up model is more likely.

The thrust nappe model is consistent with the model proposed by Grantham et al. (2008, 2013, 2019) for Balchenfjella in the eastern SRM, based on the geology of western DML and Africa. In their model, it is suggested that ~ 580–540 Ma orthogneiss terranes (e.g., the Nampula Terrane) structurally underlie ~ 630–600 Ma metamorphic complexes (e.g., the Pan-African upper nappe; Engvik et al., 2019). Such structural relationships between rocks with different metamorphisms are similar to those observed in the outcrops we studied. Of course, it will be necessary in the future to identify several other outcrops with similar relationships, and to understand their extent. If such a boundary relationship is found to be widespread in the SRM, the ductile shear zone that bounds the pelitic gneisses and the orthogneisses in the outcrop we studied may prove to be part of the plate boundary that records a continental collision at ~ 570–550 Ma. Since the metamorphism at ~ 650–600 Ma in the SRM is also thought to have been formed by collision-induced thrust movements, based on the *P*–*T* path and age of granulite-facies metamorphic rocks (Adachi et al., 2013a; Osanai et al., 2013), the results of our study show that the SRM records two collisional events at ~ 650–600 Ma and ~ 570–550 Ma.

On the other hand, Jacobs et al. (2020) and Wang et al. (2020) proposed a single continental collision, based on an analysis of igneous rocks in the SRM and the central DML. They reported differences in the timing of igneous activities and source materials between the two areas, and they suggested that the two areas were formed in different subduction systems and did not begin to behave as a single block of crust until after ~ 550 Ma. Wang et al. (2020) reported juvenile isotopic compositions in the ~ 640–600 Ma Dufek Granite in the SW Terrane, and they suggested that there was little involvement of old crustal materials in the formation of the granite. They also considered all the metamorphic rocks and meta-TTG in the SW Terrane of the SRM to be components of TOAST, and therefore TOAST had been in an oceanic arc setting isolated from continents between ~ 1000 Ma and ~ 600 Ma, followed by reworking during the closure of the Mozambique Ocean. However, the Dufek Granite has a shoshonitic composition (Wang et al., 2020) and contains ~ 950 Ma inherited zircons (Elburg et al., 2016), which indicates that it was formed by the re-melting of juvenile crust composed of TOAST. Moreover, this granite intrudes metamorphic rocks that contain detrital zircons as old as 2630 Ma (Kitano et al., 2016). These data suggest that the tectonic set-

ting in which the Dufek Granite formed was not necessarily an oceanic arc and was not isolated from older continental crust at the time of its intrusion. The widespread ~ 650–600 Ma metamorphic rocks in the SRM are interpreted to have been formed by collision of the NE and SW Terranes during the period 650–600 Ma (Osanai et al., 2013). In particular, metamorphic rocks in the NE Terrane contain detrital zircons older than 1200 Ma (Kitano et al., 2016), and sometimes older than 3000 Ma (Shiraishi et al., 2008; Osanai et al., 2013), whereas metamorphic rocks in the SW Terrane do not. These observations indicate that the 650–600 Ma event was associated with a collision between clearly different geological terranes, not a reworking within a single geological terrane. These observations suggest that the model of the entire SRM being formed during a single crustal collision at ~ 550 Ma (Jacobs et al., 2020; Wang et al., 2020) cannot explain all the key data and at present we consider a two-stage collision to be a more suitable model for the formation of the SRM.

The thrust nappe boundary between the pelitic gneisses and the orthogneisses in the outcrops of Oyayubi ridge is the first report of such a boundary in the SRM. If such a boundary were to be found over a wide area of the SRM, the tectonics of the entire SRM could be explained by thrust nappe movements that occurred during two collisional events at ~ 650–600 Ma and ~ 570–550 Ma. With regard to possible tectonic models for the final stages of formation of the Gondwana supercontinent, our results support the idea of a two-stage amalgamation, as proposed by Meert (2003).

ACKNOWLEDGMENTS

We would like to thank the members of the 61st Japan Antarctic Research Expedition, and the crew of the icebreaker 'Shirase'. We also thank A. Hubert and members of the Belgian Antarctic Research Station (2019–2020) for supporting our fieldwork. Members of the JARE geology community are thanked for fruitful discussions and support during the fieldwork in the SRM. T.A appreciates Prof. Tomokazu Hokada giving advice on the application of two feldspar thermometer. We are grateful to Prof. Joachim Jacobs and an anonymous reviewer for constructive reviews to improve the manuscript and Prof. Tomokazu Hokada for editorial handling. This study was part of the Science Program of the Japanese Antarctic Research Expedition (JARE) supported by the National Institute of Polar Research (NIPR) under MEXT. This study was financially supported by the NIPR General Collaboration Project (No. 28–25) to T.K.

SUPPLEMENTARY MATERIALS

Supplementary Tables S1–S4 are available online from https://doi.org/10.2465/jmps.230220.

REFERENCES

Adachi, T., Hokada, T., Osanai, Y., Toyoshima, T., et al. (2010) Titanium behavior in quartz during retrograde hydration: Occurrence of rutile exsolution and implications for metamorphic processes in the Sør Rondane Mountains, East Antractica. Polar Science, 3, 222–234.

Adachi, T., Hokada, T., Osanai, Y., Nakano, N., et al. (2013a) Contrasting metamorphic records and their implications for tectonic process in the central Sør Rondane Mountains, eastern Dronning Maud Land, East Antarctica. In Antarctica and Supercontinent Evolution (Harley, L.S., Fitzsimons, I. and Zhao, Y. Eds.). Geological Society of London, Special Publications, 383, 113–133.

Adachi, T., Osanai, Y., Hokada, T., Nakano, N., et al. (2013b) Timing of metamorphism in the central Sør Rondane Mountains, eastern Dronning Maud Land, East Antarctica: Constrains from SHRIMP zircon and EPMA monazite dating. Precambrian Research, 234, 136–160.

Asami, M. and Shiraishi, K. (1987) Kyanite from the western part of the Sør Rondane Mountains, East Antarctica. Proceedings of the NIPR Symposium on Antarctic Geosciences, 1, 150–168.

Asami, M., Osanai, Y., Shiraishi, K. and Makimoto, H. (1992) Metamorphic evolution of the Sør Rondane Mountains, East Antarctica. In Recent Progress in Antarctic Earth Science (Yoshida, Y., Kaminuma, K. and Shiraishi, K. Eds.). Terrapub, Tokyo, 7–15.

Asami, M., Suzuki, K. and Grew, E.S. (2005) Monazite and zircon dating by the chemical Th-U-total Pb isochron method (CHIME) from Alasheyev Bight to the Sør Rondane Mountains, East Antarctica: a reconnaissance study of the Mozambique suture in eastern Queen Maud Land. Journal of Geology, 113, 59–82.

Baba, S., Osanai, Y., Nakano, N., Owada, M., et al. (2013) Counterclockwise P–T path and isobaric cooling of metapelites from Brattnipene, Sør Rondane Mountains, East Antarctica: Implications for a tectonothermal event at the proto-Gondwana margin. Precambrian Research, 234, 210–228.

Bhadra, S. and Bhattacharya, A. (2007) The barometer tremolite + tschermakite + 2 albite = 2 pargasite + 8 quartz: Constraints from experimental data at unit silica activity, with application to garnet-free natural assemblages. American Mineralogist, 92, 491–502.

Black, L.P., Kamo, S.L., Allen, C.M., Aleinikoff, J.N., et al. (2003) TEMORA 1: A new zircon standard for Phanerozoic U-Pb geochronology. Chemical Geology, 200, 155–170.

Bohlen, S.R., Montana, A. and Kerrick, D.M. (1991) Precise determinations of the equilibria kyanite ⇌ sillimanite and kyanite ⇌ andalusite and a revised triple point for Al_2SiO_5 polymorphs. American Mineralogist, 76, 677–680.

Elburg, M., Jacobs, J., Andersen, T., Clark, C., et al. (2015) Early Neoproterozoic metagabbro-tonalite-trondhjemite of Sør Rondane (East Antarctica): Implications for supercontinent assembly. Precambrian Research, 259, 189–206.

Elburg, M., Andersen, T., Jacobs, J., Läufer, A., et al. (2016) One Hundred Fifty Million Years of Intrusive Activity in the Sør

Rondane Mountains (East Antarctica): Implications for Gondwana Assembly. The Journal of Geology, 124, 1-26.

Engvik, A.K., Tveten, E. and Solli, A. (2019) High-grade metamorphism during Neoproterozoic to Early Palaeozoic Gondwana assembly, exemplified from the East African Orogen of northeastern Mozambique. Journal of African Earth Sciences, 151, 490-505.

Fuhrman, M.L. and Lindsley, D.H. (1988) Ternary-feldspar modeling and thermometry. American Mineralogist, 73, 201-215.

Grantham, G.H., Macey, P.H., Ingram, B.A., Roberts, M.P., et al. (2008) Terrane correlation between Antarctica, Mozambique & Sri Lanka; comparisons of Geochronology, Lithology, Structure and Metamorphism and possible implications for the geology of southern Africa and Antarctica. In Geodynamic Evolution of East Antarctica: a Key to the East-West Gondwana Connection (Satish-Kumar, M., Motoyoshi, Y., Osanai, Y., Hiroi, Y., et al. Eds.). Geological Society of London, Special Publications, 308, 91-119.

Grantham, G.H., Macey, P.H., Horie, K., Kawakami, T., et al. (2013) Comparison of the metamorphic history of the Monapo complex, northern Mozambique and Balchenfjella and Austhameren areas, Sør Rondane, Antarctica: Implications for the Kuunga orogeny and the amalgamation of N and S. Gondwana. Precambrian Research, 234, 85-135.

Grantham, G.H., Kramers, J.D., Eglington, B. and Burger, E.P. (2019) The Ediacarian-Cambrian uplift history of western Dronning Maud Land: New ^{40}Ar–^{39}Ar and Sr/Nd data from Sverdrupfjella and Kirwanveggan, the source of the Urfjell Group and tectonic evolution of Dronning Maud Land within the Kuunga Orogeny and Gondwana amalgamation. Precambrian Research, 333, 105444.

Griffin, W.L., Powell, W.J., Pearson, N.J. and O'Reilly, S.Y. (2008) GLITTER: Data reduction software for laser ablation ICP-MS. Mineralogical Association of Canada Short Course Series, 40, 204-207.

Guidotti, C.V. and Dyar, M.D. (1991) Ferric iron in metamorphic biotite and its petrologic and crystallochemical implications. American Mineralogist, 76, 161-175.

Higashino, F., Kawakami, T., Satish-Kumar, M., Ishikawa, M., et al. (2013) Chlorine-rich fluid or melt activity during granulite facies metamorphism in the late Proterozoic to Cambrian continental collision zone-an example from the Sør Rondane Mountains, East Antarctica. Precambrian Research, 234, 229-246.

Higashino, F., Kawakami, T., Tsuchiya, N., Satish-Kumar, M., et al. (2019) Brine infiltration in the middle to lower crust in a collision zone: Mass transfer and microtexture development through wet grain-boundary diffusion. Journal of Petrology, 60, 329-358.

Higashino, F. and Kawakami, T. (2022) Ultrahigh-temperature metamorphism and melt inclusions from the Sør Rondane Mountains, East Antarctica. Journal of Mineralogical and Petrological Sciences, 117, 010.

Higashino, F., Kawakami, T., Adachi, T. and Uno, M. (2023) Multiple post-peak metamorphic fluid infiltrations in southern Perlebandet, Sør Rondane Mountains, East Antarctica. Journal of Mineralogical and Petrological Sciences, 118, S004.

Hokada, T., Adachi, T., Osanai, Y., Nakano, N., et al. (2022) Formation of corundum in direct contact with quartz and biotite in clockwise P-T trajectory from the Sør Rondane Mountains, East Antarctica. Journal of Mineralogical and Petrological Sciences, 117, 008.

Holdaway, M.J. (2000) Application of new experimental and garnet margules data to the garnet-biotite geothermometer. American Mineralogist, 85, 881-892.

Holdaway, M.J. (2001) Recalibration of the GASP Geobarometer in Light of Recent Garnet and Plagioclase Activity Models and Versions of the Garnet-Biotite Geothermometer. American Mineralogist, 86, 1117-1129.

Holland, T. and Blundy, J. (1994) Non-ideal interactions in calcic amphiboles and their bearing on amphibole-plagioclase thermometry. Contributions to Mineralogy and Petrology, 116, 433-447.

Ishikawa, M., Kawakami, T., Satish-Kumar, M., Grantham, G.H., et al. (2013) Late Neoproterozoic extensional detachment in eastern Sør Rondane Mountains, East Antarctica: Implications for the collapse of the East African Antarctic Orogen. Precambrian Research, 234, 247-256.

Ishizuka, H., Suzuki, S. and Kojima, H. (1996) Meta-ultramafic rock from the Austkampane area of the Sør Rondane Mountains, East Antarctica. Proceedings of the NIPR Symposium on Antarctic Geosciences, 9, 40-48.

Jacobs, J. and Thomas, R.J. (2004) Himalayan-type indenter-escape tectonics model for the southern part of the late Neoproterozoic-early Paleozoic East African-Antarctic Orogen. Geology, 32, 721-724.

Jacobs, J., Elburg, M., Läufer, A., Kleinhanns, I.C., et al. (2015) Two distinct Late Mesoproterozoic/Early Neoproterozoic basement provinces in central/eastern Dronning Maud Land, East Antarctica: The missing link, 15-21° E. Precambrian Research, 265, 249-272.

Jacobs, J., Mikhalsky, E., Hejes-Kunst, F., Läufer, A., et al. (2020) Neoproterozoic geodynamic evolution of easternmost Kalahari: Constraints from U-Pb-Hf-O zircon, Sm-Nd isotope and geochemical data from the Schirmacher Oasis, East Antarctica. Precambrian Research, 342, 105553.

Johannes, W. (1984) Beginning of melting in the granite system Qz-Or-Ab-An-H2O. Contributions to Mineralogy and Petrology, 86, 264-273.

Kamei, A., Horie, K., Owada, M., Yuhara, M., et al. (2013) Late Proterozoic juvenile arc metatonalite and adakitic intrusions in the Sør Rondane Mountains, eastern Dronning Maud Land, Antarctica. Precambrian Research, 234, 47-62.

Kawakami, T., Higashino, F., Skrzypek, E., Satish-Kumar, M., et al. (2017) Prograde infiltration of cl-rich fluid into the granulitic continental crust from a collision zone in East Antarctica (Perlebandet, Sør Rondane Mountains). Lithos, 274-275, 73-92.

Kawakami, T., Adachi, T., Uno, M., Higashino, F., et al. (2020) Report on geologic field survey in the Sør Rondane Mountains, eastern Dronning Maud Land 2019-2020 (JARE-61). Antarctic Record, 64, 351-398.

Kitano, I., Osanai, Y., Nakano, N. and Adachi, T. (2016) Detrital zircon provenances for metamorphic rocks from southern Sør Rondane Mountains, East Antarctica: A new report of Archean to Mesoproterozoic zircons. Journal of Mineralogical and Petrological Sciences, 111, 118-128.

Kojima, S. and Shiraishi, K. (1986) Note on the geology of the western part of the Sør Rondane Mountains, East Antarctica. Memoirs of National Institute of Polar Research, Special Issue, 43, 116-131.

Leake, B.E., Woolley, A.R., Arps, C.E.S., Birch, W.D., et al. (1997) Nomenclature of amphiboles; Report of the subcommittee on amphiboles of the international mineralogical association commission on new minerals and mineral names. Min-

eralogical Magazine, 61, 295-310.
Liou, J.G. (1973) Synthesis and stability relations of epidote, Ca2Al2FeSi3O12 (OH). Journal of Petrology, 14, 381-413.
Liou, J.G., Kim, H.S. and Maruyama, S. (1983) Prehnite-epidote equilibria and their petrologic applications. Journal of Petrology, 24, 321-342.
Ludwig, K.R. (2012) User's Manual for Isoplot 3.75. A Geological Toolkit for Microsoft Excel Berkeley Geochronology Center Special Publication, 5, pp.75.
McDonough, W.F. and Sun, S.-s. (1995) The composition of the Earth. Chemical Geology, 120, 223-253.
Meert, J.G. (2003) A synopsis of events related to the assembly of the eastern Gondwana. Tectonophysics, 362, 1-40.
Mieth, M., Jacobs, J., Ruppel, A., Damaske, D., et al. (2014) New detailed aeromagnetic and geological data of eastern Dronning Maud Land: Implications for refining the tectonic and structural framework of Sør Rondane, East Antarctica. Precambrian Research, 245, 174-185.
Mindaleva, D., Uno, M., Higashino, F., Nagaya, T., et al. (2020) Rapid fluid infiltration and permeability enhancement during middle-lower crustal fracturing: Evidence from amphibolite-granulite-facies fluid-rock reaction zones, Sør Rondane Mountains, East Antarctica. Lithos, 372-373, 105521.
Nakamura, D. (2009) A new formulation of garnet-clinopyroxene geothermometer based on accumulation and statistical analysis of a large experimental data set. Journal of Metamorphic Geology, 27, 495-508.
Nakano, N., Osanai, Y., Kamei, A., Satish-Kumar, M., et al. (2013) Multiple thermal events recorded in metamorphosed carbonate and associated rocks from the southern Austkampane region in the Sør Rondane Mountains, East Antarctica: A protracted Neoproterozoic history at the Gondwana suture zone. Precambrian Research, 234, 161-182.
Nakano, N., Osanai, Y., Owada, M., Binh, P., et al. (2021) Evolution of the Indochina block from its formation to amalgamation with Asia: Constraints from protoliths in the Kontum massif, Vietnam. Gondwana Research, 90, 47-62.
Newton, R.C. and Perkins, D. (1982) Thermodynamic calibration of geobarometers based on the assemblage garnet-plagioclase-orthopyroxene-(clinopyoxene)-quartz. American Mineralogist, 67, 268-286.
Osanai, Y., Shiraishi, K., Takahashi, Y., Ishizuka, H., et al. (1992) Geochemical characteristics of metamorphic rocks from the central Sør Rondane Mountains, East Antarctica. In Recent Progress in Antarctic Earth Science (Yoshida, Y., Kaminuma, K. and Shiraishi, K. Eds.). TERRAPUB, Tokyo, 17-27.
Osanai, Y., Shiraishi, K., Takahashi, Y., Ishizuka, H., et al. (1996) Geological map of the Brattnipene, Antarctica. Antarctic Geological Map Series, Sheet 34, Scale 1:50,000 National Institute of Polar Research, Tokyo.
Osanai, Y., Nogi, Y., Baba, S., Nakano, N., et al. (2013) Geologic evolution of the Sør Rondane Mountains, East Antarctica: Collision tectonics proposed based on metamorphic processes and magnetic anomalies. Precambrian Research, 234, 8-29.
Otsuji, N., Satish-Kumar, M., Kamei, A., Tsuchiya, N., et al. (2013) Late-Tonian to early-Cryogenian apparent depositional ages for metacarbonate rocks from the Sør Rondane Mountains, East Antarctica. Precambrian Research, 234, 257-278.
Owada, M., Baba, S., Osanai, Y. and Kagami, H. (2008) Geochemistry of post-kinematic mafic dykes from central to eastern Dronning Maud Land, East Antarctica: evidence for a Pan-African suture in Dronning Maud Land. In Geodynamic Evolution of East Antarctica: A Key to the East-West Gondwana Connection (Satish-Kumar, M., Motoyoshi, Y., Osanai, Y., Hiroi, Y., et al. Eds.). Geological Society of London, Special Publications, 308, 235-252.
Owada, M., Kamei, A., Horie, K., Shimura, T., et al. (2013) Magmatic history and evolution of continental lithosphere of the Sør Rondane Mountains, eastern Dronning Maud Land, East Antarctica. Precambrian Research, 234, 63-84.
Paces, J.B. and Miller, Jr, J.D. (1993) Precise U-Pb ages of Duluth complex and related mafic intrusions, northeastern Minnesota: Geochronological insights to physical, petrogenetic, paleomagnetic, and tectonomagmatic processes associated with the 1.1 Ga midcontinent rift system. Journal of Geophysical Research, 98, 13997-14013.
Shiraishi, K., Asami, M., Ishizuka, H., Kojima, H., et al. (1991) Geology and metamorphism of the Sør Rondane Mountains, East Antarctica. In Geological Evolution of Antarctica (Thomson, M.R.A., Crame, J.A. and Thomson, J.W. Eds.). Cambridge University Press, Cambridge, 77-82.
Shiraishi, K., Osanai, Y., Ishizuka, H. and Asami, M. (1997) Geological map of the Sør Rondane Mountains, Antarctica. - Antarctic geological map series, sheet 35, scale 1:250,000. National Institute of Polar Research, Tokyo.
Shiraishi, K., Dunkley, D.J., Hokada, T., Fanning, C.M., et al. (2008) Geochronological constraints on the Late Proterozoic to Cambrian crustal evolution of eastern Dronning Maud Land, East Antarctica: a synthesis of SHRIMP U-Pb age and Nd model age data. In Geodynamic Evolution of East Antarctica: A Key to the East-West Gondwana Connection (Satish-Kumar, M., Motoyoshi, Y., Osanai, Y., Hiroi, Y., et al. Eds.). Geological Society of London, Special Publications, 308, 21-67.
Spear, F.S., Kohn, M.J. and Cheney, J.T. (1999) P-T paths from anatectic pelites. Contributions to Mineralogy and Petrology, 134, 17-32.
Stern, R.J. (1994) Arc assembly and continental collision in the Neoproterozoic East African Orogen: implications for the consolidation of Gondwanaland. Annual Review of Earth and Planetary Sciences, 22, 319-351.
Tomkins, H.S., Powell, R. and Ellis, D.J. (2007) The pressure dependence of the zirconium-in-rutile thermometer. Journal of Metamorphic Geology, 25, 703-713.
Toyoshima, T., Osanai, Y., Baba, S., Hokada, T., et al. (2013) Sinistral transpressional and extensional tectonics in Dronning Maud Land, East Antarctica, including the Sør Rondane Mountains. Precambrian Research, 234, 30-46.
Tsukada, K., Yuhara, M., Owada, M., Shimura, T., et al. (2017) A low-angle brittle shear zone in the western Sør Rondane Mountains, Dronning Maud Land, East Antarctica — implication for assembly of Gondwanaland. Journal of Geodynamics, 111, 15-30.
Uno, M., Okamoto, A. and Tsuchiya, N. (2017) Excess water generation during reaction-inducing intrusion of granitic melts into ultramafic rocks at crustal P-T conditions in the Sør Rondane Mountains of east Antarctica. Lithos, 284-285, 625-641.
Wang, C.C., Jacobs, J., Elburg, M.A., Läufer, A., et al. (2020) Late Neoproterozoic-Cambrian magmatism in Dronning Maud Land (East Antarctica): U-Pb zircon geochronology, isotope geochemistry and implications for Gondwana assembly. Precambrian Research, 350, 105880.
Whitney, D.L. and Evans, B.W. (2010) Abbreviations for names of rock-forming minerals. American Mineralogist, 95, 185-187.
Wiedenbeck, M., Allé, P., Corfu, F., Griffin, W.L., et al. (1995)

Three natural zircon standards for U–Th–Pb, Lu–Hf, trace element and REE analyses. Geostandards Newsletter, 19, 1–23.
Zack, T., Moraes, R. and Kronz, A. (2004) Temperature dependence of Zr in rutile: Empirical calibration of a rutile thermometer. Contributions to Mineralogy and Petrology, 148, 471–488.

Manuscript received February 20, 2023
Manuscript accepted August 18, 2023
Advance online publication August 30, 2023
Released online publication October 11, 2023
Manuscript handled by Tomokazu Hokada